PHYSICAL REVIEW B VOLUME 50, NUMBER 13 1 OCTOBER 1994-I

Femtosecond time-resolved spectroscopy of soft modes in structural phase transitions of perovskites

Thomas P. Dougherty, Gary P. Wiederrecht, and Keith A. Nelson
Department of Chemistry, Massachusetts Institute of Technology, Cambridge, Massachusetts 02139

Mark H. Garrett and Hans P. Jenssen
Center for Materials Science and Engineering, Massachusetts Institute of Technology, Cambridge, Massachusetts 02139

Cardinal Warde
Department of Electrical Engineering and Computer Science, Massachusetts Institute of Technology, Cambridge, Massachusetts 02139

(Received 12 September 1991; revised manuscript received 9 May 1994)

Femtosecond time-domain observations of soft-mode dynamics in crystals near structural phase transitions have been conducted. Impulsive stimulated Raman scattering (ISRS) experiments are reported for both the orthorhombic phase of $KNbO_3$ and the tetragonal phase of $BaTiO_3$. The data from potassium niobate clearly show a heavily damped soft mode of B_2 symmetry and relaxational modes of A_1 symmetry but not B_2 symmetry. Similarly, the data from barium titanate clearly show a heavily damped E-symmetry soft mode and no relaxational modes of this symmetry. The absence of relaxational modes of the same symmetries as the soft modes is consistent with an eight-site order-disorder model of the phase transitions in this crystal class. The present results demonstrate significant advantages of ISRS over conventional Raman spectroscopy of low-frequency, heavily damped soft modes.

I. INTRODUCTION

The study of polarization dynamics in crystals near structural phase transitions has been conducted almost exclusively through frequency-resolved spectroscopic methods, especially light and neutron scattering. Raman spectroscopy has been particularly widely used to examine soft zone-center optic-phonon modes and slow relaxational ("hopping") modes characteristic of displacive and order-disorder transitions, respectively. However, soft modes typically become very strongly damped or overdamped as well as low in frequency near the phase-transition temperature T_c. The result is that the distinct Stokes and anti-Stokes Raman features whose frequency shifts and widths yield quantitative values for the frequencies and dephasing rates of lightly damped modes broaden and often merge into a single central peak. In this case the Raman spectral response can be very difficult to distinguish from that of a relaxational mode. Parasitic scattering contributions very near zero-frequency shift, or the filtering measures sometimes taken to remove them, can add to the difficulty. In addition, most phase transitions have both displacive and order-disorder character so that it is unclear *a priori* whether the central peak should have contributions from heavily damped soft vibrational modes, relaxational modes, or both. In these cases unique analysis of the broad central feature is often impossible. Lack of information about order-parameter dynamics prevents elucidation of the crystalline potential-energy surface along which ions or molecules move in the transformation between phases. This information is an essential ingredient for both a quantitative description and a qualitative microscopic model of a structural phase transition.

The transformations in the barium titanate family of perovskites rank among the most extensively studied of all structural phase transitions,[1] because of fundamental interest in these materials as prototype ferroelectrics and because of their widespread applications in nonlinear optics and electrooptics. Nevertheless, basic questions persist about the microscopic mechanism for the succession of phase transitions between cubic, tetragonal, orthorhombic, and rhombohedral phases. The extent of order-disorder versus displacive character and the types of motions taking place at the transitions remain in dispute. The uncertainty is due largely to the strongly damped character of the order parameter and the difficulty inherent in analysis of the Raman spectra.

Here we report the first femtosecond time-resolved impulsive stimulated Raman-scattering (ISRS) observations of soft vibrational and relaxational mode dynamics in crystals near structural phase transitions. Through ISRS experiments with the appropriate scattering symmetries, we are able to observe distinct time-dependent responses due to the heavily damped, soft polar optic-phonon modes $KNbO_3$ and $BaTiO_3$. We are also able to observe the responses of polar relaxational modes with a different scattering symmetry in $KNbO_3$. These low-frequency vibrational and relaxational modes mediate the polarization (i.e., order parameter) dynamics associated with the structural phase transitions.

For the case of potassium niobate, experiments were performed in the orthorhombic phase where questions have centered around the B_2-symmetry Raman spectrum. Preliminary ISRS results from $KNbO_3$ have been reported.[2] The B_2-symmetry Raman spectra reveal scattering features from a heavily damped soft mode, interpreted in terms of vibrational motion of the central Nb ion along the *b* crystallographic direction.[3] This is suggestive of a displacive transition in which the local potential-energy minimum for the ion shifts along the *b* direction to reach the low-temperature rhombohedral phase. (See. Figs. 1 and 2). However, the A_1 symmetry spectra show a central peak attributed to relaxational modes. These features suggest hopping of the central ion along crystallographic directions orthogonal to *b* to reach distinct local potential-energy minima which are characteristic of order-disorder rather than displacive transitions. The combination of motions may be explained qualitatively in terms of an eight-site order-disorder model which can account for partially displacive character.[3] The model is described in more detail below. However, a quantitative description of the orthorhombic-rhombohedral and other transitions of $KNbO_3$ has been frustrated by discrepancies between the temperature-dependent values of the low-frequency dielectric constant $\varepsilon_b(0)$ determined through capacitance measurements[4] and the values determined [through the Lyddane-Sachs-Teller (LST) relation] from the polar soft-mode parameters. These discrepancies have given rise to a widespread belief in the existence of additional polar modes, of relaxational origin, which have gone undetected in the low-frequency B_2-symmetry spectrum. Such modes could easily be obscured by the soft-mode spectral response, and their contributions to the dielectric constant could explain the conflicting values of $\varepsilon_b(0)$. Indeed, one Raman study reported direct observation of a relaxational as well as soft vibrational mode of B_2 symmetry.[5] Inclusion of both modes in the LST calculation yielded good agreement with the values of $\varepsilon_b(0)$ determined independently. However, a relaxational mode of B_2 symmetry is incompatible with the eight-site model. Thus, quantitative description along these lines must be accompanied by revision at a basic level of the qualitative microscopic picture.

The situation is similar for $BaTiO_3$. A displacive model[6,7] for its transitions is suggested by the temperature dependence of a soft polar optic-phonon mode,[8–14] as in $KNbO_3$. In the tetragonal phase studied here, the soft mode is of *E* symmetry, indicating twofold degeneracy and interpreted in terms of vibrational motion of the Ti ion along the (equivalent) *x* and *y* crystallographic axes. Also similar to the $KNbO_3$ case, Raman spectra of A_1 symmetry reveal relaxational contributions attributed to hopping motions of the Ti ion between distinct potential-energy minima located in different positions along the orthogonal (z) crystallographic axis.[3] Again the eight-site model offers an attractive qualitative rationalization of the data, and again quantitative description of the transitions has been frustrated by discrepancies in the low-

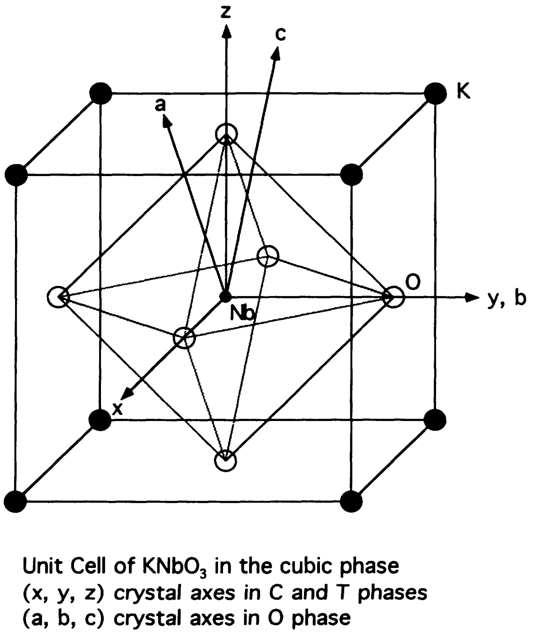

FIG. 1. Unit cell of $KNbO_3$ in the high-temperature cubic phase. The crystal axes in the cubic and tetragonal phases correspond to the (x,y,z) coordinate system. The crystal axes in the orthorhombic phase correspond to the (a,b,c) coordinate system.

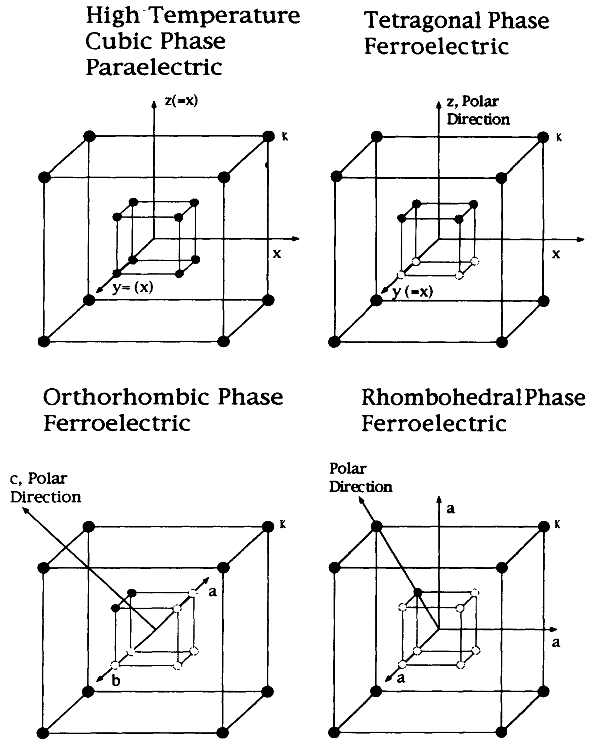

FIG. 2. Schematic illustration of the Nb-ion occupation sites within the framework of the eight-site model for $KNbO_3$ in each phase. The solid circles represent the lowest-energy (allowed) sites for the Nb ion and the open circles represent higher-energy sites. The sites are displaced from the center along the ⟨111⟩ axes, toward the corners of the unit cell. The polar axis is shown for each of the ferroelectric phases and is derived from the average position of the Nb ion in a given phase. The polar axis is not representative of a crystallographic axis in the lowest-temperature rhombohedral phase, and hence the crystallographic axes of this phase are not indicated.

frequency dielectric constants [$\varepsilon(0)$ in the cubic phase and $\varepsilon_\perp(0)$ and $\varepsilon_\parallel(0)$ in the tetragonal phase, where the subscripts indicate directions relative to the polar (z) axis]. The dielectric constant values determined through capacitance measurements[15,16] have differed substantially from those deduced through spectroscopic measurements of optic mode frequencies[8-14] and use of the Lyddane-Sachs-Teller (LST) relation. The results of many other experiments also point to an order-disorder component to the $BaTiO_3$ transitions. X-ray scattering experiments[17,18] in both crystals indicate disorder in all but the rhombohedral phases. In the cubic phase of $BaTiO_3$, anomalous temperature dependence in the refractive index[19] and symmetry-forbidden frequency doubling[20] and Raman scattering[21] all suggest that regions of tetragonal "precursor" order exist in the cubic phase and that the phase transition into the tetragonal phase has order-disorder character.

An additional factor in these materials is the mixed phonon-polariton character of the elementary excitations in near-forward-scattering experiments. In the polariton (low wave vector) region, the vibrational frequencies and damping rates are highly dispersive, and light-scattering measurements at several wave-vector magnitudes q are necessary to determine the uncoupled phonon frequencies and damping rates. At large (90°) Raman-scattering angles the soft mode is examined outside of the polariton region, where the frequency and damping rate are essentially wave-vector independent. This may appear to be a simplification in that the uncoupled phonon parameters may be determined from a single measurement at one large scattering angle. However, the damping rate increases monotonically with wave vector (as will be shown below) and the very strong damping at large wave vector results in a broad central peak in the Raman spectrum rather than distinct Stokes and anti-Stokes scattering features. In this case the frequency and damping rate are extremely difficult to determine uniquely. This accounts for the wide range of values for these parameters that have been reported.[3,5,12-14] Raman-scattering or ISRS experiments at several wave vectors are more likely to yield reliable results.

We have carried out femtosecond time-resolved ISRS experiments on $KNbO_3$ in the orthorhombic phase and $BaTiO_3$ in the tetragonal phase, in each case examining lattice responses of different symmetries and various wave-vector magnitudes. The goals have been to answer unambiguously the qualitative questions of soft-mode and relaxational mode symmetries and to determine accurate quantitative values of the soft- and relaxational mode parameters. The qualitative information is essential for an understanding of the structure of the local potential-energy surfaces in which the central ions move. The quantitative information provides a detailed description of the potential-energy surfaces, and permits reliable comparison of dielectric constant values determined from lattice dynamics and from capacitive measurements. Clarification of the symmetries of the soft and relaxational modes and reconciliation of the dielectric constant discrepancies could lead to a consistent qualitative and quantitative description of the phase transitions in this crystal class in terms of a simple and physically appealing model.

II. BACKGROUND

A. The barium titanate family of crystals

The phase-transition temperatures in $KNbO_3$ have been found to be 701, 488, and 210 K on cooling and 704, 493, and 265 K on heating.[22] For $BaTiO_3$, the phase-transition temperatures are 403, 278, and 183 K.[1] All three transitions in both crystals show significant first-order character as can be seen from thermal hysteresis. The transitions were initially described[1,6,7] as displacive, with cooperative motion taking place along a soft lattice vibrational coordinate. Further experiments[2-5,17-21,23-25] demonstrated that a purely displacive model was incomplete and that some order-disorder character must be included.

The soft-mode model of structural phase transitions[6,7] predicts that, at each phase transition, the frequency of the soft normal mode decreases as the transition temperature is approached from above or below. A mean-field description yields the following temperature dependence:

$$\omega_s^2 = A(T-T_c) , \tag{1}$$

where A is a constant and T_c is the second-order transition temperature. The Lyddane-Sachs-Teller (LST) relation for one optic mode,

$$\varepsilon_0 = \varepsilon_\infty \frac{\omega_{\mathrm{LO}}^2}{\omega_{\mathrm{TO}}^2} \tag{2}$$

gives the low-frequency dielectric constant ε_0 as a function of the high-frequency dielectric constant ε_∞ and the frequencies of the longitudinal (LO) and transverse (TO) optic phonons. The soft mode is a transverse optic phonon, and if ε_∞ and ω_{LO}^2 are approximately temperature independent, Eqs. (1) and (2) indicate a divergence in ε_0 as the transition temperature is approached, i.e.,

$$\varepsilon_0 = \frac{C}{|T-T_c|} , \tag{3}$$

where C is the Curie constant.

Infrared and Raman spectroscopic studies of $KNbO_3$ show[3,5,22,23] that as each phase transition is approached from above, a zone-center phonon decreases in frequency as the soft-mode model predicts. Just below the two higher-temperature transitions, however, the soft-mode frequency does not increase as indicated by Eq. (1) but instead continues to decrease. Only after the orthorhombic-rhombohedral transition does the soft-mode frequency increase. Given this temperature dependence of the soft mode, the divergence of the low-frequency dielectric constant predicted by Eq. (3) should only be observed at the orthorhombic-rhombohedral transition; ε_0 should increase continuously as the temperature is lowered through the first two transitions. Dielectric measurements, on the other hand, show divergences of ε_0 at all three phase transitions.[4,24,25] The temperature dependencies of the phonon frequencies are unable to account for the divergence of ε_0 near the two higher-temperature transitions.[22] The contribution from an order-disorder polarization relaxation mechanism with a characteristic frequency (i.e., hopping rate) below optic-phonon frequencies could account for the discrepancy between the low-frequency dielectric constant values obtained from capacitance measurements and LST values deduced from phonon frequencies obtained through spectroscopic experiments. The generalized LST relation, including contributions from n vibrational modes and m relaxational modes with lifetimes τ, has the following form:

$$\varepsilon_0=\varepsilon_\infty \prod_{i=1}^{m} \frac{\tau_{Ti}}{\tau_{Li}} \prod_{j=1}^{n} \frac{\omega_{Lj}^2}{\omega_{Tj}^2} \ . \tag{4}$$

The existence of an order-disorder mode is also suggested by diffuse x-ray scattering[17,18] which is observed from all but the rhombohedral phase. This indicates that all phases are partially disordered except for the rhombohedral phase.

The crystal structure of the prototype cubic phase and the 45° rotation of the crystal axes in the orthorhombic phase are indicated in Fig. 1. The tetragonal phase has crystal axes along the same directions as in the cubic phase. The existence and the pattern of diffuse scattering from the three highest-temperature phases have been interpreted in terms of an "eight-site" model[17,18] in which it is proposed that eight local potential-energy minima for the central ion lie in off-center sites along the $\langle 111 \rangle$ axes, between the unit-cell center and the cations at the eight corners. In the high-temperature phase, all the sites are degenerate and the average symmetry is cubic. In the tetragonal phase, four sites in a plane are lower in energy than the other four; in the orthorhombic phase, two adjacent sites are allowed and there are two sets of higher-energy sites (twofold and fourfold degenerate); and in the rhombohedral phase, only one site is allowed. A schematic illustration of the eight-site model is shown in Fig. 2. This model is consistent with many experimental results and also with the results of computer simulations of $KNbO_3$ which indicate that in the orthorhombic phase, the Nb ion is found primarily in two adjacent $\langle 111 \rangle$ sites.[26]

The eight-site model is an order-disorder model. In general, this would suggest thermally assisted hopping dynamics of the central ion among the allowed and higher-energy sites and therefore relaxational order parameter dynamics. However, if the potential-energy barrier between allowed sites is low compared to the zero-point energy of vibration about the potential-energy minima, then motion between allowed sites is vibrational in character while motion between allowed and higher-energy sites remains relaxational. In this manner, illustrated in Fig. 3, the eight-site model can account for both relaxational and soft vibrational components of the polarization.

Two groups have reported low-frequency light-scattering (LS) spectra from the orthorhombic phase of $KNbO_3$. Sokoloff *et al.*[3] found that a single, heavily damped soft vibrational mode (i.e., a heavily damped harmonic oscillator) could account well for the B_2-symmetry spectrum. This result led to the proposal, described above, of a double-well potential with a very low barrier separating the two allowed sites. The low-frequency A_1-symmetry spectrum was described by two relaxation times, and modeled by a strongly asymmetric double-well potential with a barrier height far above the zero-point energy for the Nb motion. The damped oscillator and relaxational modes appeared in scans of different symmetry and were attributed to motions of the Nb ion along different axes.

Note that these LS results and the eight-site model suggest that the relaxational motions should contribute to low-frequency dielectric constant components to which the soft mode does not contribute, e.g., $\varepsilon_z(0)$ in the tetragonal phase and $\varepsilon_a(0)$ and $\varepsilon_c(0)$ in the orthorhombic phase. The heavily damped soft mode in the orthorhombic phase should influence the $\varepsilon_b(0)$ dielectric constant as discussed above. This dielectric component should not show any effects of relaxational modes.

Fontana *et al.*[5] pointed out that the soft-mode frequencies deduced from the B_2-symmetry Raman spectra of Sokoloff *et al.* could not account through the LST relation for the behavior of the $\varepsilon_b(0)$ dielectric constant as determined through capacitance measurements. They reported B_2-symmetry spectra which appeared to contain contributions from both the heavily damped soft mode

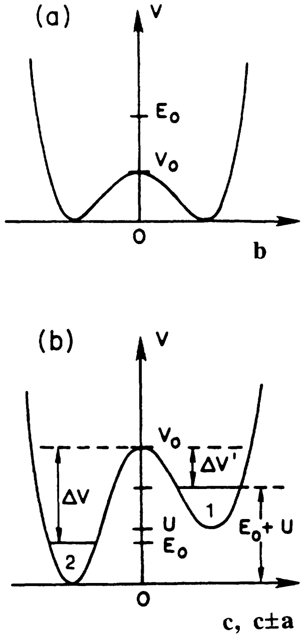

FIG. 3. Proposed potential-energy surfaces for Nb-ion motion in the orthorhombic phase, adapted from Ref. 3. (a) The two lowest-energy sites are separated by a barrier whose height is below the zero-point energy. Damped vibrational motion takes place along this direction. (b) Four sites lie at a higher energy than the allowed sites, and two sites lie at a higher energy still. The asymmetric double-well potentials are sketched. Hopping motion takes place between the allowed sites and these sites, giving rise to the two relaxational features seen in A_1-symmetry data.

and a coupled relaxational response. The generalized LST relation yielded good agreement with the $\varepsilon_b(0)$ dielectric measurements when both modes were considered. The results were explained in terms of a six-site order-disorder model with Nb ion moving among wells occupying off-center sites along the $\langle 100 \rangle$ axes. Subsequent analysis by Sokoloff *et al.* led to the suggestion that the apparent relaxational contributions to the B_2-symmetry spectrum were in fact due to parasitic scattering. However, this analysis did not reconcile the discrepancies in $\varepsilon_b(0)$ values.

In $BaTiO_3$, a similar discrepancy between dielectric constant values led to the widespread belief that there must be additional low-frequency relaxational modes which are obscured by the soft-mode contribution to the E-symmetry Raman spectrum.

B. Impulsive stimulated light scattering

The experimental method used is femtosecond time-resolved "impulsive" stimulated Raman scattering (ISRS), in which ultrashort excitation pulses exert a sudden ("impulse") driving force on Raman-active modes and the resulting phase-coherent nuclear motion is monitored through coherent scattering of variably delayed, ultrashort probe pulses. In the time-delayed four-wave mixing or "transient grating" experimental configurations used, ISRS data should contain the same information concerning lattice dynamics as conventional Raman spectra recorded with the same wave vector and polarization combinations. ISRS data from an underdamped phonon mode show time-dependent oscillations whose period and decay rate correspond to the lineshift and linewidth, respectively, of the associated Raman spectral feature. For a relaxational response, ISRS data show a time-dependent decay whose rate corresponds to the Raman central peak linewidth. In general, the ISRS signal $S(t)$ is described in scalar form by [27]

$$S(t) \propto |G^{\varepsilon\varepsilon}(t)|^2 , \tag{5}$$

where $G^{\varepsilon\varepsilon}(t)$ is the dielectric constant impulse response function (Green's function) whose Fourier transform is probed in spontaneous light-scattering (LS) spectroscopy. The Stokes and anti-Stokes LS spectral intensities are given by

$$S(\omega) \propto \begin{Bmatrix} n(\omega)+1 \\ n(\omega) \end{Bmatrix} \mathrm{Im}[G^{\varepsilon\varepsilon}(\omega)] , \tag{6}$$

where $n(\omega)$ is the Bose-Einstein thermal factor,

$$n(\omega) = (e^{\hbar\omega/k_B T} - 1)^{-1} . \tag{7}$$

In either ISRS or LS components of the tensor quantity $G^{\varepsilon\varepsilon}$ are selected by appropriate choice of incident and signal polarizations. Limitations in time or frequency resolution are neglected in Eqs. (5) and (6), but finite pulse durations are accounted for in the ISRS data analysis below. The dynamics observed through ISRS or Raman spectroscopy are related to the (uncoupled[27]) material modes α, described by response functions $G^\alpha(t)$ or $G^\alpha(\omega)$, through the Raman-scattering differential polarizabilities $a_{ij}^\alpha = \partial\varepsilon_{ij}/\partial Q^\alpha$, where Q^α is displacement along normal coordinate α:

$$G_{ij}^{\varepsilon\varepsilon} = \sum_\alpha a_{ij}^\alpha G^\alpha . \tag{8}$$

In practice, certain material responses may be viewed more clearly in either the time or frequency domain. Impulsive stimulated scattering (ISS) has proved particularly useful for observation of modes with low-frequencies and/or high damping rates, and for separation of relaxational and low-frequency oscillatory modes whose quasielastic LS spectral signatures overlap. Variation of the light-scattering angle, and particularly the use of small angles, is also facilitated in ISS. ISS has been applied to the observation of soft acoustic phonons in crystals near structural phase transitions,[28] shear and longitudinal acoustic waves in glass-forming liquids,[29] and local intermolecular vibrations in simple liquids.[30]

In the perovskites studied here, the issue of low-frequency spectral content is one for which time-domain techniques are well suited. Since the phonon frequencies are low (<100 cm^{-1}), the time resolution required (about 100 fs) is readily achievable. Most importantly, the temporal profile of ISRS data is not distorted by elastically scattered light and so low-frequency features are not obscured. Excessive elastic scattering of excitation and probe pulses by a sample of poor optical quality (due to domain walls, impurities, or other causes) can reduce the signal-noise level of ISRS data in a uniform way, but does not preferentially contribute to one temporal region of the data. This is in contrast to LS spectra in which elastically scattered light contributes most heavily to the low-frequency region, and thus leads to distortion of the frequency-dependent response.

III. EXPERIMENT

A. ISRS spectroscopy measurements

A synchronously pumped and amplified femtosecond dye laser, similar to one which has been described in detail elsewhere, was used.[30] The system consists of a cw mode-locked Nd:YAG laser whose frequency-doubled output pumps an antiresonant ring femtosecond dye laser. The 615-nm, 70-fs dye laser pulses are amplified in three stages by the frequency-doubled output of a Q-switched, mode-locked and cavity-dumped Nd:YLF laser whose output is synchronized to that of the Nd:YAG laser through a common mode-locker rf source.[31] Superior mode quality, pointing stability, and peak power make Nd:YLF advantageous to Nd:YAG for this application. The Nd:YLF cavity includes a cylindrical lens to compensate for the natural astigmatism of YLF, and is designed for optimal mode size at the rod to produce the most energy without sacrificing stability.[32] Small spot sizes at the ends of the cavity allow for efficient mode locking. To avoid optical damage to the $LiNbO_3$ Pockels' cell used for cavity dumping, the output pulse energy is limited to 1 mJ. The amplified dye laser output, after double-passing through a prism pair to compensate for dispersion, consists of 70-fs pulses with 6 μJ per pulse at a 350 -Hz repetition rate.

The amplified output is split into two equal-energy excitation pulses and a weaker probe pulse. The excitation pulses are spatially and temporally overlapped in the sample to "impulsively" drive LS-active material modes. The geometry of the crossed excitation pulses relative to the crystallographic axes determined the scattering wave vector. The probe beam is variably delayed along a stepping-motor delay line with a resolution of 1 μm and incident on the sample at the phase-matching (Bragg) angle for coherent scattering. The intensity of coherently scattered light is measured as a function of probe delay to provide the ISRS signal. The output voltage from the signal detector and from a diagnostic detector which monitors the amplified pulse energy were digitized and stored after each laser shot. If the amplified pulse energy did not fall within 15% of the average energy, the signal for that shot was discarded. At each point on the delay line, signals from approximately 500 repetitions of the excitation-probe sequence were averaged.

The polarizations and orientations of the pump beams determined the symmetry and wave vector of the excitations produced in the sample. The Raman activity of the optic modes in an orthorhombic crystal of $KNbO_3$ are determined by the symmetry elements of the C_{2v} point group. In order to generate pure A_1 excitations, the pump geometry shown in Fig. 4(a), $a-\Delta b(cc)a+\Delta b$, with a scattering angle of 5.27° was used. In this notation, the beam propagation directions are indicated outside the parentheses and the beam polarizations are indicated inside. The resulting excitations were polarized along the c axis with the wave vector parallel to the b axis. The same $a-\Delta b(cc)a+\Delta b$ geometry was used for the probe and scattered beams. Pure B_2 excitations were produced with the geometry $a-\Delta c(bc)a+\Delta c$ for the pump beams [see Figs. 4(b)]. The excitations were polarized along the b axis with the wave vector in the ac plane. Again, the same geometry was used for the probe and scattered light. The B_2 experiments were performed over a range of wave vectors to examine polariton dispersion. Scattering angles of 1.53°, 2.60°, 3.97°, 8.03°, and 11.9° were used. Note that the scattering angle is defined as the angle between the excitation pulses in air.

The Raman activities of the optic modes in the tetragonal phase of $BaTiO_3$ are determined by the symmetry elements of the C_{4v} point group. For generation of pure A_1 excitations, the pump geometry of $x-\Delta y(zz)x+\Delta y$, was used with a scattering angle of 5.27°. The resulting excitations were polarized along the z axis with the wave vector parallel to the y axis. The same geometry was used for the probe and scattered beams. Transverse E-symmetry excitations were produced with the geometry $x-\Delta y(yz)x+\Delta y$ for the two pump beams. The polarization and the wave vector were in the xy plane. E-symmetry longitudinal optic phonons were not excited impulsively because their frequencies are too high. The same $x-\Delta y(yz)x+\Delta y$ geometry was used for the probe and scattered light. The E-symmetry experiments were performed over a range of wave vectors to examine polariton dispersion. Scattering angles (measured in air) of 0.52°, 1.68°, 3.60°, 5.27°, and 7.53° were used.

A 4×4×1 mm single-domain crystal of orthorhombic $KNbO_3$, with the a crystallographic axis perpendicular to the large face and the b and c axes parallel to the edges of the large face, was obtained from Virgo Optics. It was grown by the Kyropolous method, x-ray oriented, poled along the c axis with 100 V/mm at 200 °C, cut and polished. The samples were mounted in an evacuated chamber, with the temperature controlled to ±20 mK by a P-I-D controller and a resistive heater. Experiments were conducted with sample temperatures in the 290–480 K range.

A 5×5×2 mm single-domain crystal of tetragonal $BaTiO_3$, with the x crystallographic axis perpendicular to the large face and the y and z axes parallel to the edges of the large face, was used. It was grown in the cubic phase by the top-seeded solution growth technique from 33.4 mol % reagent grade barium carbonate and 66.6 mol % titanium dioxide of 99.999% purity. Single crystals were made from x-ray oriented samples that were etched in the cubic phase to eliminate surface stresses that limit the movement of domain walls. The crystals were electrically poled at 129 °C, just below the transition into the tetrago-

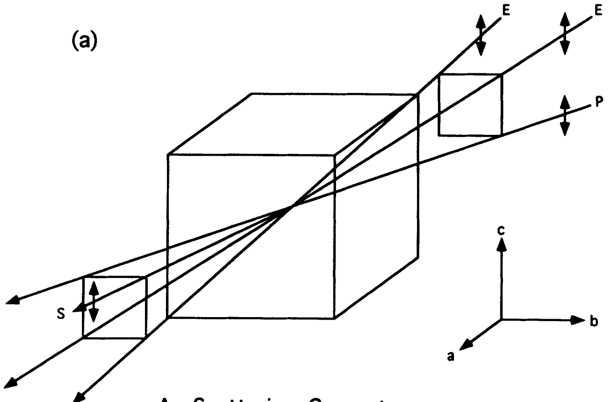

A_1 Scattering Geometry

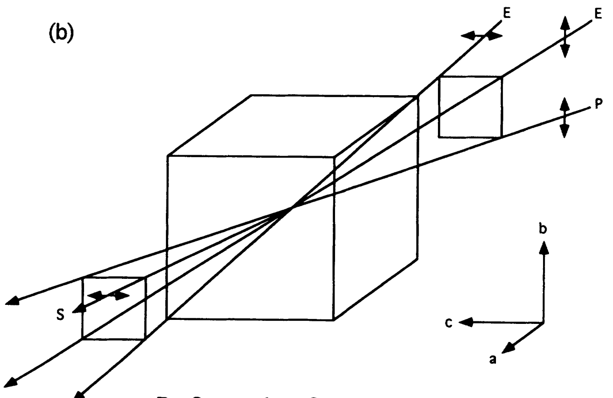

B_2 Scattering Geometry

FIG. 4. The scattering geometries for the A_1 (a) and B_2 (b) experiments. In both cases there are two excitation pulses (E), one probe pulse (P) and one scattered pulse (S). The polarizations of the pulses are marked with double-headed arrows. The (a,b,c) coordinate system corresponds to the crystal orientation.

nal phase at 130.5 °C, to form single domains. The x faces were polished to an optical quality finish with diamond paste on an optical flat. The optical extinction coefficient was measured to be smaller than 1×10^{-5} at 633 nm. Experiments were conducted with sample temperatures in the 286–392 K range.

B. Calculation of the scattering wave vector

The scattering wave-vector magnitude $|\mathbf{q}|=q$ can be determined from the excitation angle θ and wavelength λ in air without knowledge of the refractive index if the excitation pulses enter the same face of the sample and are polarized parallel to each other and along a pure mode direction of the crystal. In that case the direction of $\mathbf{q}$ is in the plane of the two pump beams and perpendicular to the line bisecting the angle between them, and its magnitude is given by the expression

$$q=\frac{4\pi\sin(\theta/2)}{\lambda} . \tag{9}$$

For perpendicularly polarized pulses, the refractive index for each polarization must be known. If the refractive indices for the two polarizations are not identical, then the magnitude and direction of $\mathbf{q}$ are different from the parallel polarized case. The component of $\mathbf{q}$ perpendicular to the line bisecting the angle between the pulses, $q_\perp$ is identical to the value of q calculated in Eq. (9). The component parallel to the bisector of θ, $q_\parallel$, is no longer zero and has the following form:

$$q_\parallel=\frac{2\pi}{\lambda}\left[\sqrt{n_1^2-\sin^2(\theta/2)}-\sqrt{n_2^2-\sin^2(\theta/2)}\right] . \tag{10}$$

The magnitude of $\mathbf{q}$ and the rotation angle ϕ of its direction from the parallel polarized case are given by the following two equations:

$$q=\sqrt{q_\perp^2+q_\parallel^2} , \tag{11}$$

$$\phi=\tan^{-1}\left[\frac{q_\parallel}{q_\perp}\right] . \tag{12}$$

Notice that this puts a lower bound on the smallest wave vector accessible through depolarized light scattering; even at $\theta=0$, $q_\parallel$ and q are not equal to zero. As the angle between the pump beams is changed both the magnitude and direction of $\mathbf{q}$ change. For $KNbO_3$, the analysis of our B_2 results obtained with different scattering angles remains relatively straightforward because the polarization of the mode is always perpendicular to $\mathbf{q}$ and so the mode is always a pure transverse B_2 excitation. Dispersion should therefore depend only on the magnitude of $\mathbf{q}$ and not on its direction in the *ac* plane. The wave vectors in $KNbO_3$ were calculated using Eqs. (9)–(12) with values of the refractive indices determined at 615 nm,[33] $n_B=2.336$ and $n_C=2.173$.

For the tetragonal crystal of $BaTiO_3$, the pump pulses are perpendicularly polarized along inequivalent (x and z) axes, the values of n_x and n_z at 615 nm are needed to calculate $q_\parallel$ as described in I, Eq. (10). However, at the small scattering angles used in these experiments, one can assume that

$$n^2\gg\sin^2(\theta/2) \tag{13}$$

and $q_\parallel$ can be approximated with the following expression:

$$q_\parallel\cong\frac{2\pi}{\lambda}(n_z-n_x)=\frac{2\pi}{\lambda}\Delta n , \tag{14}$$

where Δn is the birefringence whose temperature dependence of 633 nm has been reported.[16] At 25 °C the ratio of Δn(615 nm):Δn(633 nm) is 1.025,[16] and this was assumed to be the case at all temperatures.

IV. EXPERIMENTAL RESULTS

A. B_2 symmetry ISRS data from potassium niobate

Light scattering by the soft transverse optic phonon has B_2 symmetry in the orthorhombic phase. Typical data are shown in Fig. 5. In these figures a very heavily damped oscillatory nuclear response is seen. There is also a contribution from the instantaneous electronic polarizability which persists only while the excitation and probe pulses are overlapped temporally inside the sample. These two features both contribute to signal near $t=0$. At all temperatures and wave vectors, the nuclear response appears to be well described in terms of a single, heavily damped harmonic oscillator. No evidence of any contribution from a relaxational mode of this symmetry is seen.

The data were analyzed in the following way. The impulse response function was assumed to have the form

$$G'^{\varepsilon\varepsilon}(t-t'\geq0)=A\delta(t-t')+Be^{-\gamma(t-t')}\sin[\omega(t-t')] \tag{15}$$

where the instantaneous electronic response to the excitation pulses (the first term) has been included along with the nuclear response (the second term). The dielectric response to excitation pulses of finite time duration is calculated by convolution of the Green's function with the excitation intensity profile $F(t)$:

$$\Delta\varepsilon(t)=\int_{-\infty}^{t}F(t')G'^{\varepsilon\varepsilon}(t-t')dt' . \tag{16}$$

The grating signal is proportional to $|\Delta\varepsilon(t)|^2$ after convolution with the probe pulse intensity profile $P(t)$:

$$S(t)\propto\int_{-\infty}^{\infty}P(t')[\Delta\varepsilon(t-t')]^2dt' . \tag{17}$$

The temporal profiles of the pump and probe pulses are approximated by Gaussians centered at $t'=0$. The first term in $G'(t-t')$ representing the purely electronic response contributes to signal only when the pump and probe pulses are all overlapped temporally in the sample. During this time, i.e., for $t<200$ fs, the convolution integral indicated in Eq. (17) is calculated numerically. After the excitation pulses have passed, only the phonon response contributes, and an analytic solution for the signal can be calculated by extending the limit of integration for $\Delta\varepsilon(t)$ to infinity. The values of the frequency ω and damping rate γ indicated in Eq. (15) were determined

TABLE I. Soft-mode frequency ω and damping rate γ of $KNbO_3$ determined from B_2-symmetry ISRS data as functions of temperature and wave-vector magnitude q. The parameters were determined through fits of the data based on Eq. (15).

Temp (K)		Wave vector (cm^{-1})				
		1.69×10^4	1.73×10^4	1.81×10^4	2.20×10^4	2.70×10^4
290.0	ω (ps^{-1})		8.12			
	γ (ps^{-1})		3.69			
347.7	ω		8.41			
	γ		4.34			
366.5	ω	8.52		8.61	8.54	8.98
	γ	4.23		4.56	4.57	5.17
395.1	ω	8.61	8.67	8.61	8.63	9.08
	γ	4.34	4.67	4.77	4.77	5.51
442.4	ω	8.90	8.87	8.84	8.72	9.00
	γ	5.06	5.09	5.27	5.37	6.14
461.4	ω	8.81	8.87	8.77	8.83	8.89
	γ	5.16	5.15	5.45	5.55	6.26
470.9	ω	8.75	8.86	8.76	8.74	8.89
	γ	5.16	5.20	5.53	5.88	6.54
480.4	ω	8.75	8.80	8.71	8.51	8.81
	γ	5.22	5.31	5.75	5.85	6.63

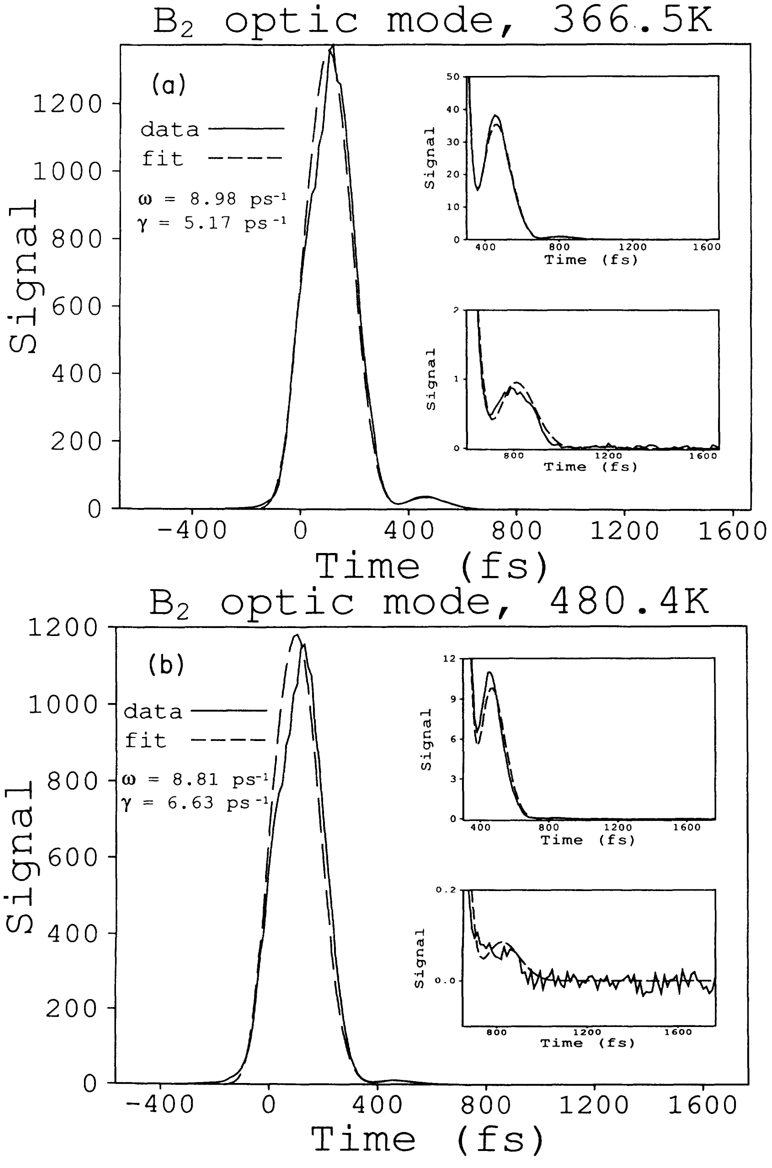

FIG. 5. B_2-symmetry ISRS data from $KNbO_3$ at 366.5 and 480.4 K showing the dynamics of the soft mode. The nuclear response at each temperature is fit well with a single-damped harmonic oscillator [Eq. (15) of the text] with the parameters indicated. These data were recorded with the largest scattering angle used, 11.9°, corresponding to a wave-vector magnitude $q=2.70\times10^4\ cm^{-1}$.

through a least-squares-fitting routine in which each data point was weighted by an estimate of the reciprocal of its uncertainty. In this manner data spanning 3 orders of magnitude in the dynamic range, showing very strongly damped oscillations, could be fit without ignoring the weaker part of the signal which still contains important information. We estimate the uncertainties in our values of ω and γ to be approximately ±5%. This value was determined by setting one of the parameters at different fixed values and repeating the fitting procedure with all other parameters allowed to vary, until acceptable fits could no longer be obtained.

The temperature and wave-vector dependencies of ω and γ obtained from ISRS experiments are indicated in Table I. The frequency shows little temperature dependence, but the damping rate rises significantly with temperature.

Figure 6 displays the wave-vector dependence of ω and γ at six of the temperatures investigated. All wave-vector magnitudes investigated, $1.69-2.70\times10^4$ cm^{-1}, are within the polariton region. Birefringence limits experiments in this configuration to wave vectors larger than 1.67×10^4 cm^{-1}. Raman-scattering experiments at a 90° angle probe higher wave vectors outside the polariton regime, yielding the phonon frequency and damping rate in the absence of coupling to light. The theoretical curves accompanying the data in Fig. 6 come from a polariton dispersion relation which is based on a single polar mode model,[34,35] in which the uncoupled phonon response function is given by

$$G(\varpi)=(\varpi^2+i\varpi\Gamma-\omega_0^2)^{-1} , \tag{18}$$

where ϖ is a complex frequency. To account for several optic modes, we treat the coupling of light to the lowest-frequency mode explicitly and assume that the contributions to the dielectric constant from higher-frequency modes may be accounted for implicitly in a modified high-frequency limiting value ε'_∞ (Ref. 35). The resulting dispersion relation is a fourth-order polynomial in ϖ:

$$\varpi^4+i\Gamma\varpi^3-\frac{c^2q^2+\omega_0^2\varepsilon_0}{\varepsilon'_\infty}\varpi^2-\frac{i\Gamma c^2q^2}{\varepsilon'_\infty}\varpi+\frac{\omega_0^2c^2q^2}{\varepsilon'_\infty}=0 . \tag{19}$$

The wave-vector-dependent roots of this equation are two pairs of complex conjugates. The lower-frequency pair of roots is directly comparable to the ω and γ measured by our experiments. The higher-frequency pair of solutions can never be below the frequency of the longitudinal optic mode frequency, which is 421 cm^{-1} in this case.[22] These describe a higher-frequency mode which cannot be detected with our pulse durations. Because of the inclusion of all higher-frequency modes in ε'_∞, the high-frequency solution is only valid at $q=0$. Calculations of phonon and dielectric properties with a more complicated dispersion relation derived by including explicitly all polar modes of B_2 symmetry have been presented elsewhere.[35] The results indicate that the lower-frequency solutions to Eq. (19) provide good approximations of the measured parameters at all wave vectors accessible to light scattering.

The dispersion relation has four parameters, ω_0, Γ, ε_0, and ε'_∞. (Note the ε_0 and ε'_∞ refer to the limiting values of the ε_b component.) ε'_∞ was calculated using the following equation:

$$\varepsilon'_\infty=\varepsilon_\infty\frac{\omega^2_{\mathrm{LO}_3}}{\omega^2_{\mathrm{TO}_3}} , \tag{20}$$

where mode 3 is the only one of the three higher-frequency B_2 optic modes that exhibits a splitting of its transverse and longitudinal frequencies and contributes to ε'_∞. The TO and LO frequencies, 516 and 820 cm^{-1}, are known from IR reflectivity measurements.[22] The value of ε_∞, 4.938, was obtained by extrapolating the two-term Sellmeier relation from refractive index data[33] to infinite wavelength. Evaluating Eq. (20) gives $\varepsilon'_\infty=12.5$. The value of ω_{LO} (421 cm^{-1}) is temperature independent.[22] Therefore, ε_0 [here $\varepsilon_0=\varepsilon_b(0)$ in Eq. (19)] can be eliminated as an independent parameter as well because the LST relation can be derived from the dispersion model. We utilize Eq. (2) with ε'_∞ replacing ε_∞ to include the contribution of the higher-frequency mode. Only ω_0 and Γ remain as adjustable parameters for fitting the dispersion relation to the data in Fig. 6, and the values used in the theoretical curves are displayed in the figure. Using the value of ω_0, we then calculate ε_0 through the LST relation. In other words, we use three equations [the complex equation (19) and the LST relation] to determine the three unknowns ω_0, Γ, and ε_0. We estimate our uncertainties in these values to be approximately ±2%. (Note that the uncertainties are lower than those for individual measurements of ω and γ since these values are calculated using many of the individual results.) These values for ω_0 and Γ are the natural frequency and damping rate for the uncoupled mode [Eq. (18)].

We have examined temperature-dependent values of $\varepsilon_b(0)$ determined through dielectric measurements[4] to see whether a consistent quantitative description of KNbO$_3$ behavior can be achieved without including any low-frequency relaxational responses of B_2 symmetry. Our

TABLE II. Values of the natural frequency ω_0 and damping rate Γ of the uncoupled soft optic mode of KNbO$_3$, determined with a damped polariton model [Eqs. (18) and (19)] from wave-vector-dependent values of ω and γ, are shown. The values of $\varepsilon_b(0)$ determined from ω_0 and the LST relation are also reported.

Temp (K)	ω_0 (ps^{-1})	Γ (ps^{-1})	ω_0 (cm^{-1})	Γ (cm^{-1})	$\varepsilon_b(0)$
290.0	10.1	9.5	53.6	50.4	770
347.7	10.7	11.2	56.8	59.4	686
366.5	10.7	11.0	56.8	58.4	686
395.1	10.9	11.6	57.8	61.5	661
442.4	11.4	13.2	60.5	70.0	604
461.4	11.4	13.4	60.5	71.1	604
470.9	11.5	13.9	61.0	73.7	594
480.4	11.5	14.1	61.0	74.8	594

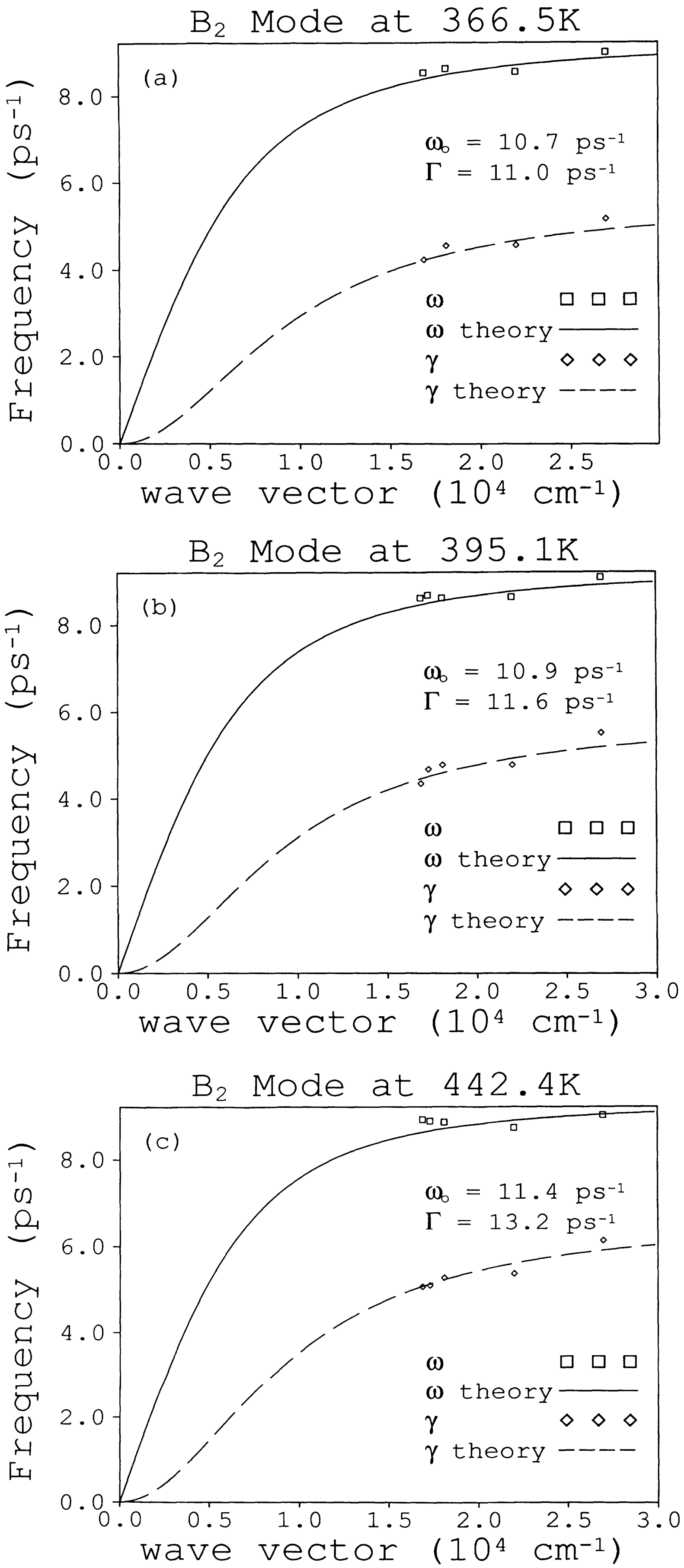

FIG. 6. The values of ω and γ, as a function of q, deduced from the B_2-symmetry spectra of $KNbO_3$ are modeled with a damped polariton model [Eq. (19)] at six temperatures. The values of ω_0 and Γ reported are the natural frequency and damping rate for the mode in the absence of coupling to light [high-q limit, Eq. (18)].

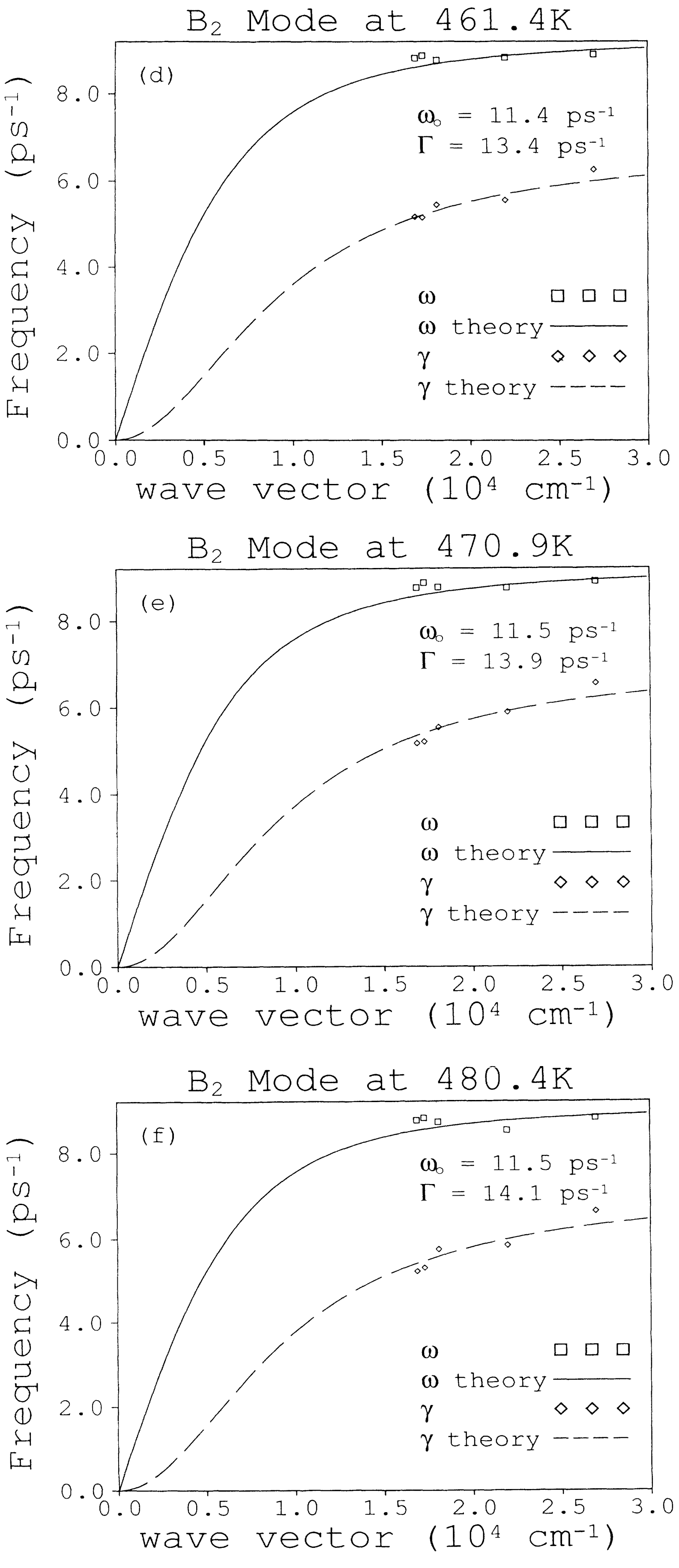

FIG. 6. (*Continued*).

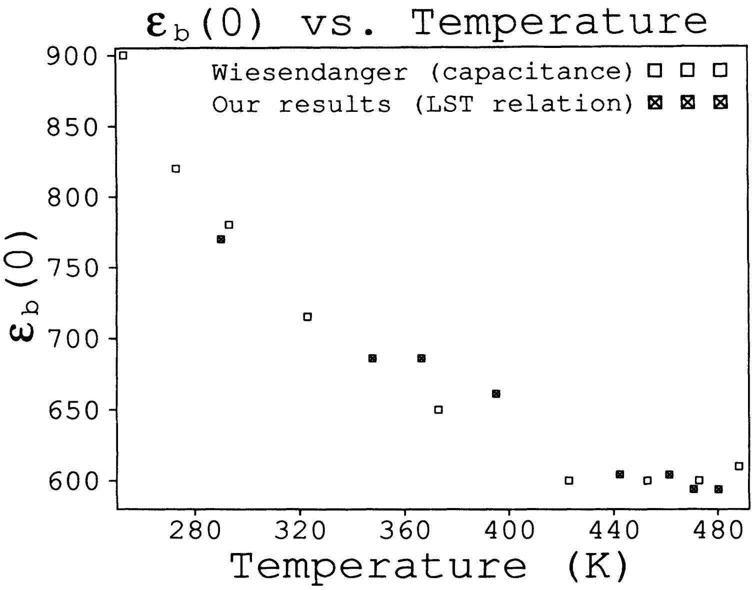

FIG. 7. The low-frequency dielectric constant of $KNbO_3$, $\varepsilon_b(0)$, calculated from the natural frequency of the soft mode and the LST relation, as a function of temperature. Also shown are the values determined from capacitance measurements in Ref. 4.

temperature-dependent values of $\varepsilon_b(0)$ were determined as described above by the LST relation and our values for ω_0. The values of $\varepsilon_b(0)$ determined in this manner were not adjusted to improve the agreement with dielectric measurements. The results of the comparison are shown in Fig. 7. The capacitance measurements were not made at a frequency above piezoelectric resonances, but the piezoelectric coupling was measured as well so the acoustic contributions to $\varepsilon_b(0)$ could be subtracted and a clamped value of $\varepsilon_b(0)$ determined. It is the clamped values of $\varepsilon_b(0)$ that can be compared meaningfully to LST values. The uncertainties in the capacitance measurements were estimated at approximately ±50. We estimate our uncertainty to be approximately ±40 except at 290 K and 347.7 K, where the uncertainty is hard to estimate because we have values of ω and γ at only one wave vector. A summary of the values of ω_0, Γ, and $\varepsilon_b(0)$ determined by our experiments is given in Table II. From the excellent agreement between values of $\varepsilon_b(0)$ deduced from our measurements and capacitance measurements, we conclude that the soft vibrational mode and higher-frequency polar modes are sufficient to account for $\varepsilon_b(0)$ in the orthorhombic phase. This result further supports the conclusion from the raw ISRS data that no B_2-symmetry relaxational response exists.

B. Effects of low-frequency relaxational contributions on ISRS data

To make clear the effects of an additional, relaxational mode on ISS data, and to provide some indication of the extent to which we can rule out such a mode, Fig. 8 shows simulated data to which both a damped oscillatory mode and a relaxational mode contribute. The ISRS sig-

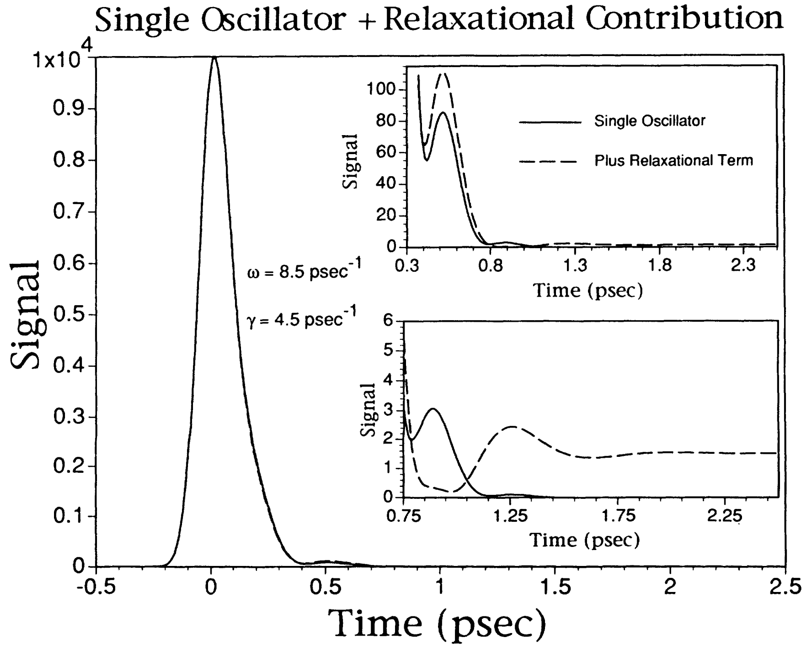

FIG. 8. Simulated ISRS soft-mode data with an additional contribution from a very weakly scattering (or very weakly coupled) relaxational mode. The parameters used are $B/A=0.01$, $\omega=8.5$ ps^{-1}, $\gamma=4.5$ ps^{-1}, and $\lambda=6.28\times10^{-4}$ ps^{-1}. Highly nonexponential decay of the oscillations is observed. This illustrates the sensitivity of the ISRS data to even a very weak contribution to signal due a relaxational mode.

nal (neglecting the electronic contribution near $t=0$) has the following form, reflecting the oscillatory and relaxational contributions:

$$S(t)\propto(Ae^{-\gamma t}\sin(\omega t)+Be^{-\lambda t})^2\ . \tag{21}$$

The relative magnitudes of A and B depend on the light-scattering cross sections of the two modes and on the extent of coupling between them. In Fig. 8, the optic mode frequency and damping rate are chosen to be similar to those found for the soft mode of $KNbO_3$. To demonstrate the extreme sensitivity of ISRS data to even a weak relaxational contribution which in the frequency domain would have an extremely narrow linewidth, the decay rate of the relaxational mode in the simulation was chosen to be only 100 MHz and the ratio of amplitudes, B/A, was chosen to be 0.01. Even with the parameters chosen, the relaxational term has a dramatic effect on the form of ISS data because of the crossterm in Eq. (21). The decay of the oscillations is highly nonexponential. After the oscillations are damped beyond the limit of experimental detectability, there is a long-lived signal component whose intensity relative to the peak intensity is roughly $(B/A)^2=10^{-4}$. We chose B/A to put this long-lived component of signal just at the limit of our experimental signal-noise level. Any significant relaxational contribution, even if weaker than the oscillatory contribution by a factor of 10^{-4}, would be easily detectable. Of course, accurate determination of a relaxation rate as low as 100 MHz would require extension of the experimental time scale all the way to the microsecond range, and this is readily achievable. However, even on the femtosecond time scale of the simulation the existence of an additional low-frequency contribution to signal can be proved with excellent sensitivity. No evidence of nonexponential decays or long-lived signal components were found in our experiments at any temperature or wave vector.

It is of some interest to examine simulated ISRS data using the soft vibrational and relaxational mode parameters reported by Fontana *et al.* who believed that contributions from both modes were present. Fontana *et al.* used a coupled-mode model (see the Appendix of Ref. 5) to fit their Raman spectra, and reported the temperature-dependence parameters (see Fig. 6 of Ref. 5). At 490 K, the values of these parameters are $\Gamma_\infty=97$ cm^{-1}, $\Omega_\infty=67.5$ cm^{-1}, $\gamma_r=9.0$ cm^{-1}, and $\delta=22.0$ cm^{-1}. It was assumed that the scattering intensity is due to the Raman activity of the soft mode, and the relaxational response is seen only through its coupling to the soft mode. The parameters above yield for our ISRS simulations the values $A/B=72.4$, $\lambda=1.48$ ps^{-1}, $\omega=8.94$ ps^{-1}, and $\gamma=9.25$ ps^{-1}. The simulated ISRS signal based on these parameters (with an instantaneous electronic response of typical intensity included at $t\approx0$) has been presented.[2] An attempt to fit this simulation to an exponentially decaying sine wave demonstrates how significantly the form of the simulation differs from our experimental results. Note that if it is assumed that the relaxational mode is also Raman active, the form of the data changes only slightly and is still very different from the damped-oscillator form observed experimentally.

C. *E* symmetry ISRS data from barium titanate

Typical *E*-symmetry data from $BaTiO_3$, recorded with three different scattering wave vectors, are shown in Figs. 9(a)–9(c). The signal includes an instantaneous response due to the electronic polarizability, which persists only while the excitation and probe pulses are overlapped temporally in the sample, and a longer-lived response due to the lattice modes. The electronic response provides a measure of the pulse duration but is of no additional interest for our purposes. The data at all temperatures examined throughout the tetragonal phase show an overdamped response at large wave vectors and an underdamped polariton response at small wave vectors. At no wave vector or temperature was any relaxational contribution to the *E*-symmetry lattice response detected. Although ISRS signal-to-noise ratios from the soft mode in $BaTiO_3$ are about tenfold weaker than those from $KNbO_3$ (mainly because of poorer $BaTiO_3$ optical quality), a relaxational mode with very weak scattering intensity or coupling would still be detectable. We estimate that, in terms of Eq. (21), a relaxational mode with amplitude ratio of $B/A=0.01$ (which would yield an uncoupled scattering intensity of 10^{-4} relative to the scattering intensity of the soft mode) would be observed.

The impulse response function describing the lattice response was assumed to have one of the following forms:

$$G'^{\varepsilon\varepsilon}(t-t'\geq0)=A\delta(t-t')+Be^{-\gamma(t-t')}\sin[\omega(t-t')] \tag{22a}$$

or

$$G'^{\varepsilon\varepsilon}(t-t'\geq0)=A\delta(t-t')+B(e^{-\lambda_1(t-t')}-e^{-\lambda_2(t-t')})\ , \tag{22b}$$

where the instantaneous electronic response to the excitation pulses (the first term) has been included along with the nuclear response (the second term). The two response functions (22a) and (22b) describe underdamped and overdamped oscillators, respectively. All the data except those from the largest scattering angle were fit using Eq. (22a). We estimate the experimental uncertainties in our values of ω and γ, when ω is greater than γ (small scattering angles), to be approximately ±5%. When γ is greater than ω (intermediate scattering angles), the uncertainty in γ is approximately ±10%. When ω is only slightly smaller than γ, the uncertainty in ω is also approximately ±10%. As ω approaches zero and the mode is nearly overdamped the relative uncertainty in ω becomes much greater than 10%, but the absolute uncertainty remains relatively constant. At the largest scattering angle, the rise of the overdamped response described mainly by λ_1 was too fast to be determined with our time resolution except at the lowest temperature studied. At the higher temperatures, λ_1 was estimated from the polariton dispersion relation (see below) and held fixed during the fitting procedure. The excellent agreement between the values of λ_1 and λ_2 at the lowest temperature where both could be determined from the data and the values calculated from the dispersion relation support

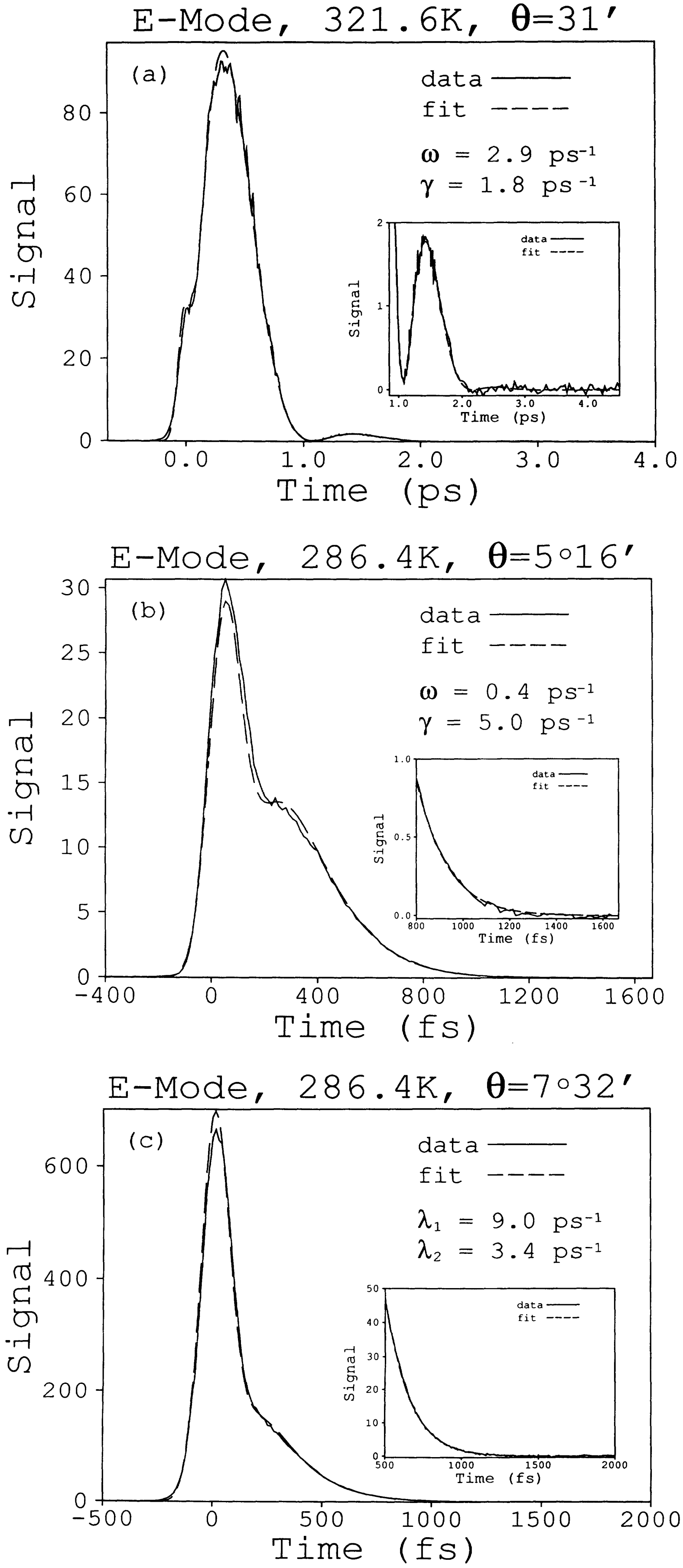

FIG. 9. E-symmetry ISRS data from $BaTiO_3$ showing the polariton dispersion of the soft mode. The nuclear response at each temperature is fit well as a single underdamped or overdamped harmonic oscillator [Eqs. (22) of the text] with the parameters indicated.

TABLE III. Soft-mode frequency ω and damping rate γ or (when overdamped) decay rates λ_1 and λ_2 of $BaTiO_3$, determined from E-symmetry ISRS experiments at different temperatures and wave-vector magnitudes q. The parameters were determined through fits of the data based on Eq. (22). Note that the values of λ_1 reported at the highest three temperatures are estimated from the dispersion relation and not measured directly.

Temp (K)		Wave vector (cm^{-1}), mode parameters (ps^{-1})				
286.4	q	5.58×10^3	6.27×10^3	8.46×10^3	1.09×10^4	1.45×10^4
	ω (or λ_2)	2.4	2.5	2.2	0.4	(3.4)
	Γ (or λ_1)	2.0	2.4	3.4	5.0	(9.0)
321.6	q	5.03×10^3	5.78×10^3	8.10×10^3	1.06×10^4	1.43×10^4
	ω	2.9	3.1	3.2	0.8	(4.2)
	γ	1.8	2.3	3.3	6.1	(12)
354.6	q	4.18×10^3	5.06×10^3	7.60×10^3	1.02×10^4	1.40×10^4
	ω	3.0	3.3	3.4	1.2	(4.7)
	γ	1.7	2.2	3.6	6.5	(12)
392.2	q	2.87×10^3	4.05×10^3	6.97×10^3	9.78×10^3	1.37×10^4
	ω	2.6	3.0	3.0	0.4	(4.5)
	γ	1.3	2.0	3.8	6.7	(12)

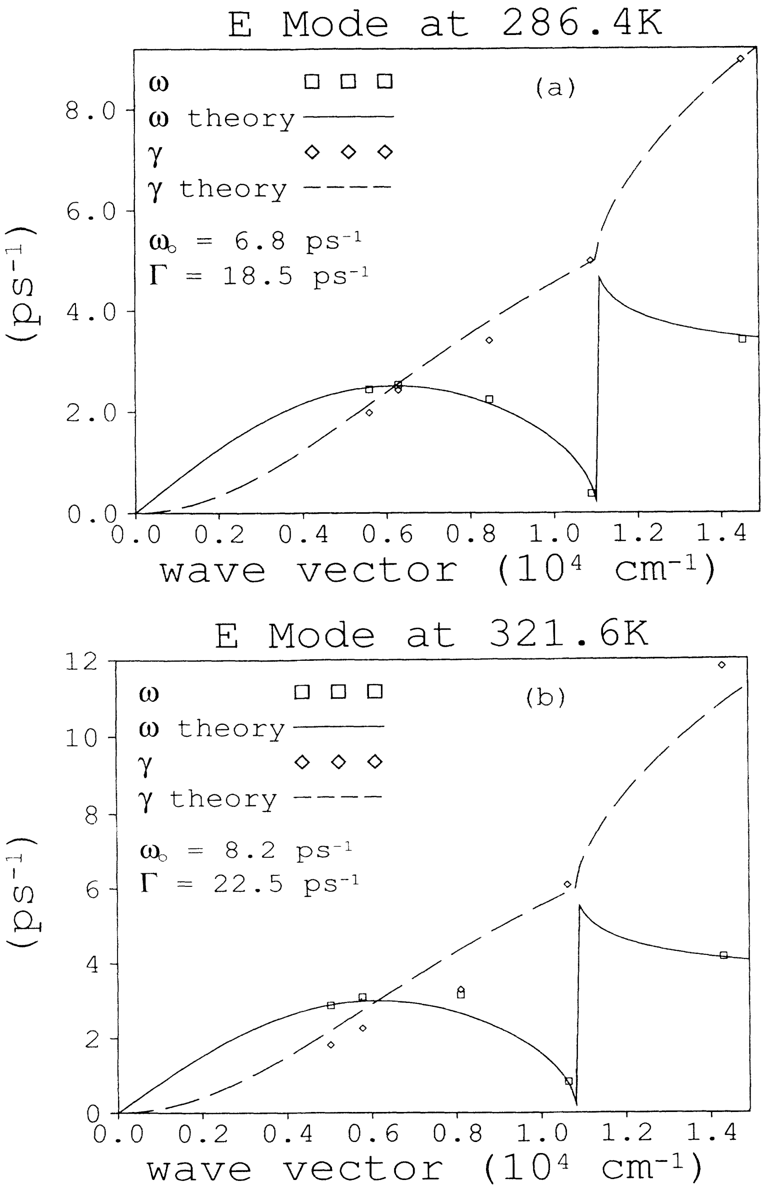

FIG. 10. The q-dependent values of ω and γ (and, at the highest wavevector, λ_1 and λ_2) for the photon-polariton mode in $BaTiO_3$ deduced from E-symmetry ISRS data at four temperatures. The solid and dashed curves give the frequencies and damping rates, respectively, expected based on a damped polariton model [Eq. (19)]. The values of ω_0 and Γ reported are the natural frequency and damping rate for the uncoupled phonon mode [high-q limit, Eq. (18)]. Note that the uncoupled mode is overdamped at all temperatures.

this assumption. If an uncertainty of 10% is assumed in the estimate for λ_1, then the uncertainty in our measurement of λ_2 which describes the decay of the overdamped response is less than 5%. The values of ω, γ, λ_1, and λ_2 at the temperatures and wave vectors examined in ISRS experiments are given in Table III.

Of the three E-symmetry optic modes, only the lowest-frequency mode (the soft mode) is sufficiently polar to make a significant contribution to the low-frequency dielectric constant.[8,9] The polariton dispersion model[34,35] discussed above is adequate to describe the data. The low-frequency solutions for $i\bar{\omega}$ are a pair of complex conjugates at small q (overdamped oscillator) and become two real roots at larger q (overdamped oscillator). As q is increased further, the two real roots approach the two exponential decay rates which describe the uncoupled overdamped oscillator at high q. We again use the two equations from the complex relation (19) and the LST relation (20) to eliminate the three unknowns ω_0, Γ, and ε_0. The value of ε_∞ can be determined from refractive index data, although as has been discussed[16] ε_∞ is not simply equal to n^2. From the limiting value of the Sellmeier relation $\lambda \to \infty$, ε_∞ is 5.22 (Ref. 16). Raman spectra collected at near-forward-scattering angles in the 6.5–40 °C temperature range demonstrated that the dispersion is consistent with the LST relation[11] (despite the discrepancy between LST and capacitance measurements of ε_0 discussed earlier). ε_0 can therefore be replaced with its LST value. From IR (Ref. 8) and Raman[12] experiments the longitudinal frequency, ω_L, is known to be approximately 710 cm^{-1}. With these substitutions for ε_0 and ε_∞ the dispersion relation has only two free parameters, ω_0 and Γ. At each temperature, the

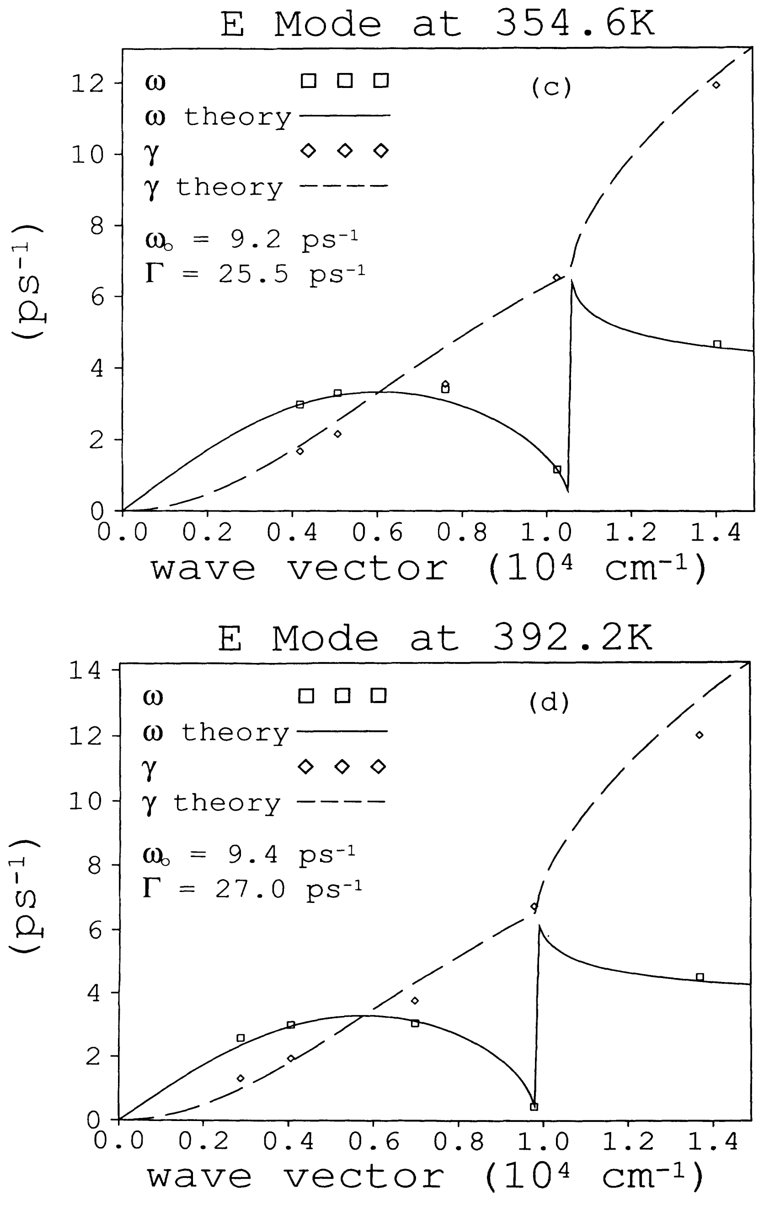

FIG. 10. (*Continued*).

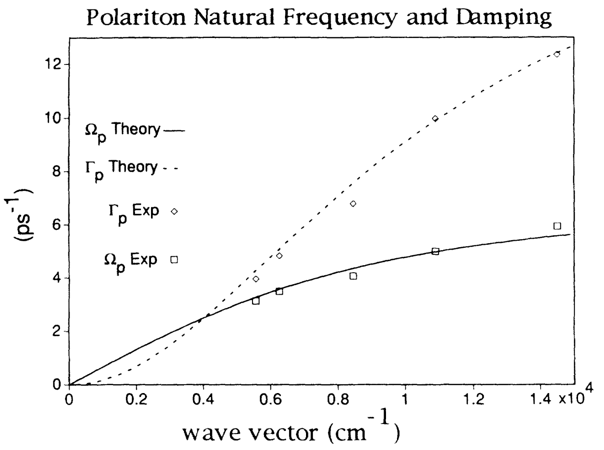

FIG. 11. A plot of the BaTiO$_3$ polariton natural frequency Ω_p and damping rate Γ_p for the data illustrated in Fig. 10(a) is shown. The curves illustrate the expected dispersion for a single polar mode.

TABLE IV. Values of the natural frequency ω_0 and damping rate Γ of the uncoupled soft optic-phonon mode of BaTiO$_3$, determined from wave-vector-dependent phonon-polariton parameters ω and γ (or λ_1 and λ_2) and the damped-polariton model of Eq. (19). The values of $\varepsilon_\perp(0)$ determined from ω_0 and the LST relation are also reported.

Temp (K)	ω_0 (ps^{-1})	Γ (ps^{-1})	ω_0 (cm^{-1})	Γ (cm^{-1})	$\varepsilon_\perp(0)$
286.4	6.8	18.5	36.1	98.1	2020
321.6	8.2	22.5	43.5	119	1390
354.6	9.2	25.5	48.8	135	1100
392.2	9.4	27.0	49.9	143	1060

values of ω_0 and Γ were adjusted to model the data at the five scattering angles examined. The results are shown in Figs. 10(a)–10(d). The discontinuity near 1.0×10^4 cm^{-1} marks the transition from an underdamped oscillator described by a frequency and a damping rate to an overdamped oscillator described by two exponential decay

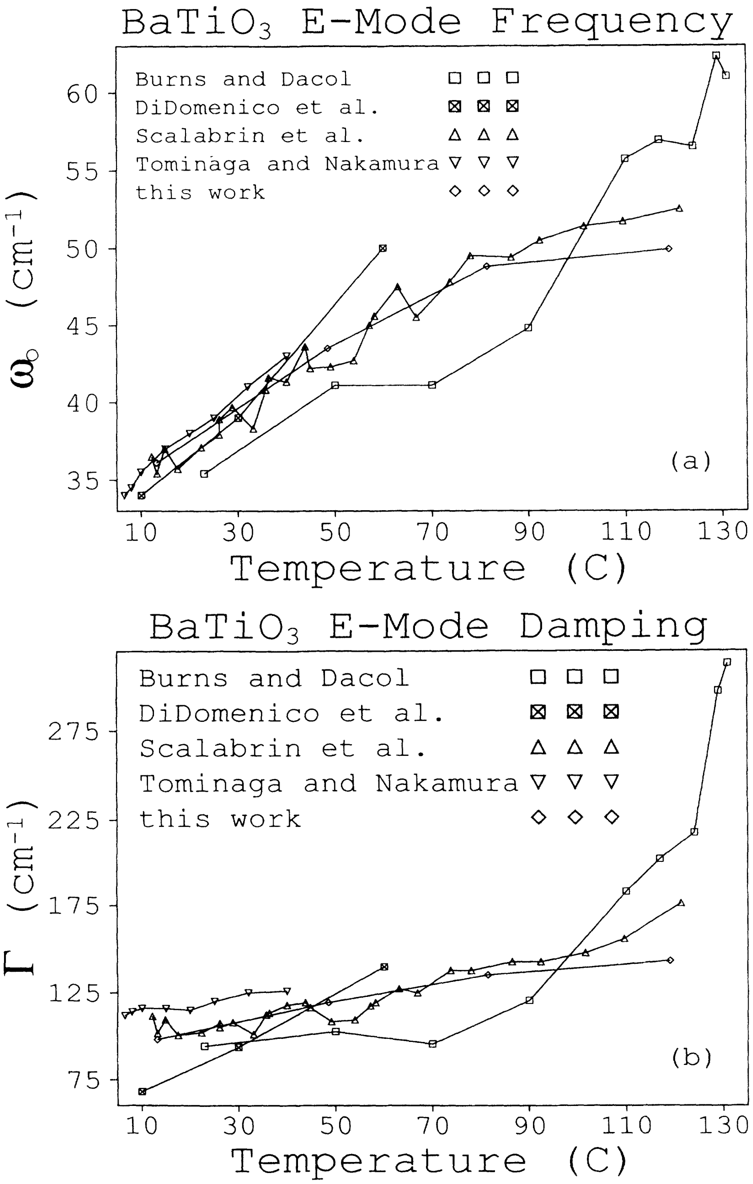

FIG. 12. The temperature dependence of the natural frequency and damping rate of the BaTiO$_3$ overdamped *E*-symmetry soft mode. Our results are compared to those reported in Refs. 11–14.

rates. The wave-vector-dependent parameters ω, γ, λ_1, and λ_2 [see Eqs. (22a) and (22b)] can be related to the q-dependent polariton natural frequency Ω_p and decay rate Γ_p as follows: $\Omega_p^2=\omega^2+\gamma^2$ or $\Omega_p^2=\lambda_1\lambda_2$, and $\Gamma_p=2\gamma$ or $\Gamma_p=\lambda_1+\lambda_2$, where the relations apply for underdamped or overdamped responses, respectively. Plots of Ω_p and Γ_p vs q do not show any discontinuity at the change from underdamped to overdamped dynamics. This is illustrated in Fig. 11, which is a plot of the predicted and experimental values of Ω_p and Γ_p for the data shown in Fig. 10(a). The discontinuities in Fig. 10(a) are qualitatively consistent with the results of previous polariton experiments.[11,36,37] The values of ω_0 and Γ determined from the dispersion curves are summarized in Table IV, and we estimate the uncertainties of these values to be ±4%. Note that these uncertainties are less than those of the parameters ω and γ (and λ_1 and λ_2) determined directly from the measurements, since those parameters at all five wave vectors are used to determine ω_0 and Γ at each temperature.

In Fig. 12, our values for the uncoupled optic mode frequency and damping rate are compared to the results of three 90° Raman experiments[12–14] which covered temperatures throughout the tetragonal phase and one near-forward-scattering (polariton regime) Raman study[11] which covered only temperatures up to 40 °C. Not included in this figure are other results[36,38,39] in which the values of ω_0 are based on the assumption of agreement between LST and capacitance measurements of the dielectric constant. The earlier results all show the same temperature-dependent trends, with a 10–25 % range of values for the frequency and a 25–100 % range for the damping rate. Our results fall within these ranges, and as indicated above we believe the uncertainties are considerably smaller than those of the 90° Raman measurements. There is good agreement at low temperatures with the small-angle Raman results[11] which should be more reliable than those at larger angles. The good agreement with one set of 90° Raman results[13] is more surprising. The difficulty of uniquely determining ω_0 and Γ for an overdamped mode is demonstrated by the scatter among the three 90° Raman results displayed in Fig. 12.

The temperature-dependent values $\varepsilon_\perp(0)$, as calculated through the LST relation, are shown in Table IV and plotted in Fig. 13. For BaTiO$_3$, large discrepancies between the values of $\varepsilon_\perp(0)$ determined from Raman spectra through the LST relation and from capacitance measurements[12] have long been noted.[11–14,36,37] Our results fall within the range of values determined earlier, and also disagree with those of earlier capacitance measurements. However, more recent capacitance measurements have been reported[40] which yield excellent agreement with our results. These and the earlier capacitance values are included in Fig. 13. A low-frequency relaxational mode of E symmetry was proposed to account for the previous differences, but such a mode has not been seen in Raman spectra[3] and appears to be ruled out based on the current results.

D. Conclusions from the soft-mode ISRS data

The results of B_2-symmetry ISRS data in KNbO$_3$ and E-symmetry data from BaTiO$_3$ show signals from a single, heavily damped soft phonon mode in each crystal at all temperatures and wave-vector magnitudes studied. The raw data alone rule out the possibility of any significant contribution from relaxational modes of the same symmetries as the soft modes. Quantitative analyses of the phonon parameters yield consistent descriptions of the phase-transition dynamics in which the temperature-dependent lattice vibrational and dielectric properties are accounted for. This further undermines support for the presence of additional relaxational modes of the soft mode symmetries.

In the case of KNbO$_3$, earlier Raman spectroscopy re-

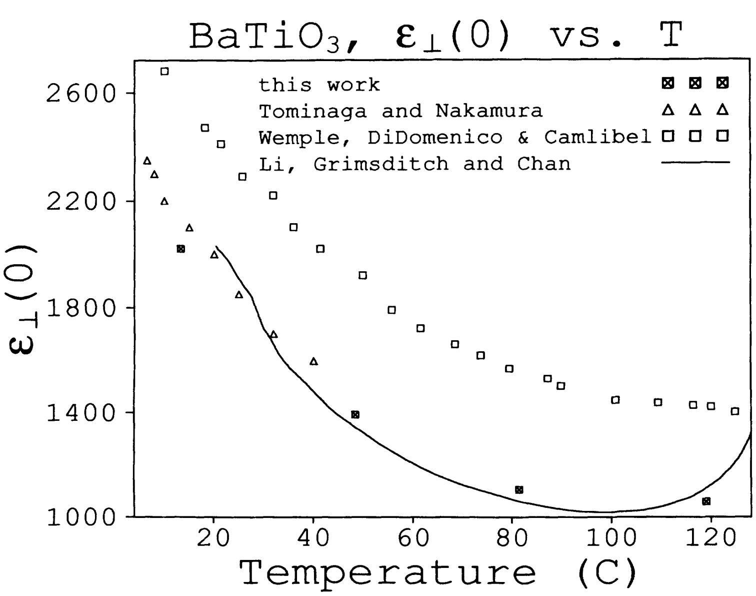

FIG. 13. The low-frequency dielectric constant $\varepsilon_\perp(0)$, calculated from the natural frequency of the soft mode and the LST relation, as a function of temperature. Also shown are the values determined from capacitance measurements in Refs. 16 and 40), and the values determined from earlier polariton experiments (Ref. 11).

sults were in dispute over the presence of a relaxational mode of B_2 symmetry. However, even the results which did not indicate such a mode yielded quantitative values of the phonon parameters ω_0 and Γ which differed from ours by 15–50%. Figure 14 shows the results of both Raman studies and the present ISRS results. (We note that Fontana *et al.* fit their results to a coupled-mode model. We have used the parameters of the uncoupled oscillator in the figure, but including the coupling only produces a renormalization of approximately 1% in the oscillatory mode parameters.) We attribute the large discrepancies among ISRS and earlier results to the difficulty of fitting the frequency-domain response uniquely.

In the case of $BaTiO_3$, Raman spectroscopy results yielded a wide range of values for the phonon parameters. The values we report fall within this range and are close to some of the values reported earlier. It is difficult for us to tell whether the close agreement of some of the earlier values is fortuitous or due to systematic improvements in the Raman spectroscopy measurements of analysis.

E. A_1 symmetry data from $KNbO_3$

A_1-symmetry Raman spectra of $KNbO_3$ indicate two relaxational features and no low-frequency vibrational modes.[3] The A_1-symmetry ISRS data from $KNbO_3$ are consistent with this. They exhibit a $t=0$ spike, due to the electronic polarizability, followed by a nuclear response which appears relaxational rather than oscillatory in character. A short-time scan of the A_1 response at 395 K, shown in Fig. 15(a), has three main features. There is the spike at $t=0$ with a width determined by the time duration of the pump and probe pulses. This is followed by an exponentially decaying signal, and finally by

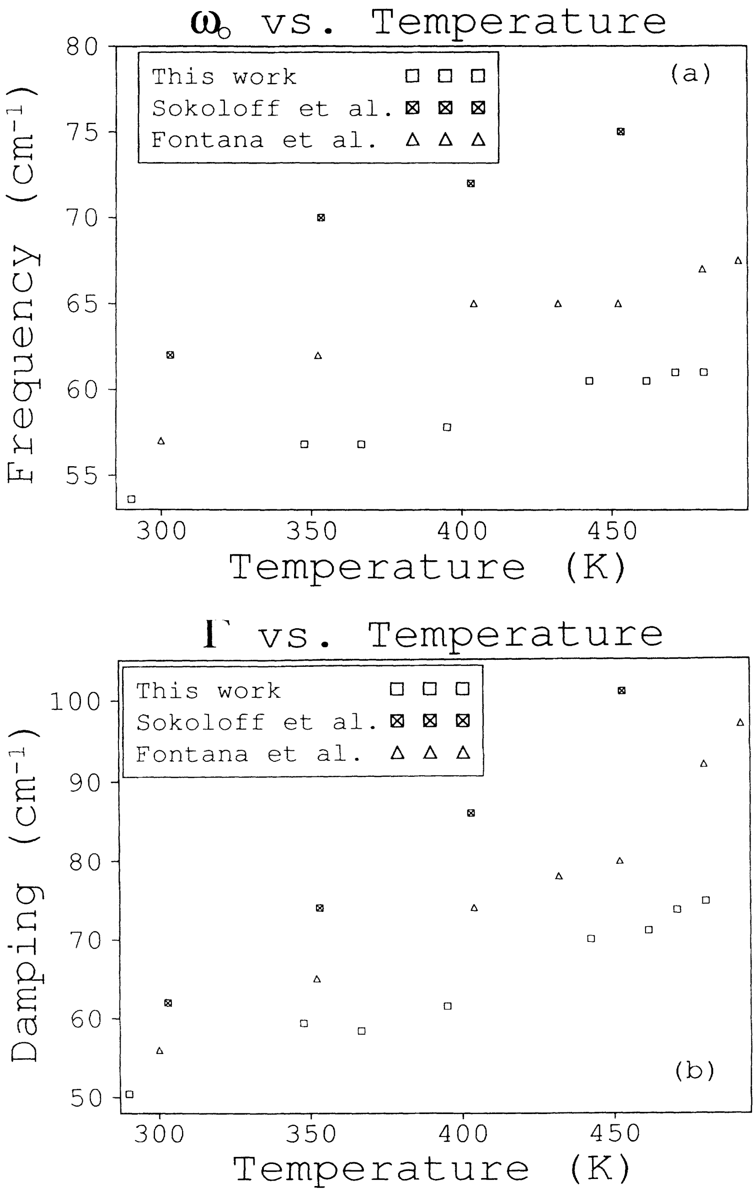

FIG. 14. The temperature dependence of the natural frequency and damping rate of the B_2-symmetry soft mode. We attribute the differences between our results and those of Raman spectra (Refs. 3 and 5) to the difficulty of fitting the latter to unique values of the soft-mode parameters.

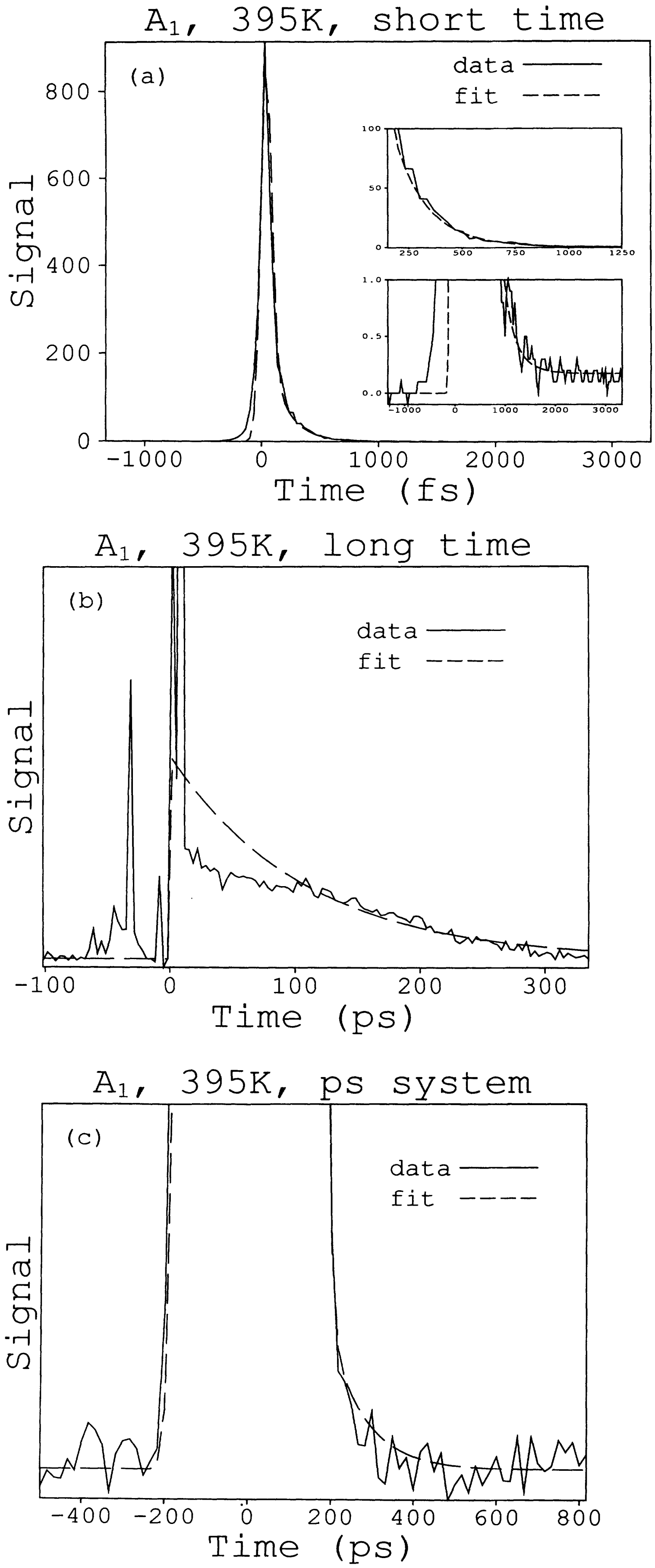

FIG. 15. A_1-symmetry ISRS data from $KNbO_3$ at 395 K. (a) shows data extending to 3 ps. The top inset shows a rapid decay of signal intensity during the first picosecond. The lower inset shows that a low signal level remains after the fast decay. (b) shows that this signal decays on a time scale of several hundred picoseconds. (c) shows data recorded with 90-ps pulses, confirming the presence of the weak, slowly decaying component of the signal.

a low baseline signal level which does not return to zero on the time scale of the data.

Figure 15(b) shows the longer time response recorded with a more sensitive detector. On this time scale, the decay of the weak feature can be observed. To protect the PMT in the long-time scans, the delay line was not stopped at $t=0$ and so there is no $t=0$ spike in this scan. The spikes are experimental artifacts, possibly due to weak satellite pulses from the dye laser. To test the reliability of the long time data, the experiment was repeated using the output of a Q-switched and mode-locked Nd:YAG laser with 90-ps pulses. The results, shown in Fig. 15(c), confirm that the long-time response measured with femtosecond pulses is real. The intensity of the long-time response is so low that a quantitative analysis is not yet possible. Relaxation times reported for the slow relaxational mode are given only as rough estimates.

The temperature dependences of the fast and slow relaxational modes determined from these data are shown in Figs. 16 and 17, respectively. Our results for the fast relaxation show the same temperature-dependent trends as those of Sokoloff *et al.*,[3] but all the values show a discrepancy of nearly a factor of 2. Both experiments would seem to have measured this response too accurately for such a difference to be attributed to uncertainty in the data. We continue to seek an explanation for the discrepancy. Meaningful comparison of the slow relaxation rates is not possible because they were not well determined from either ISS or LS data, in the former case because of the weak signal intensity and in the latter case because the linewidth was comparable to that of the I_2 absorption filter.

In Ref. 3, the A_1 relaxational response was analyzed in terms of the eight-site model. The potential energy surface for Nb-ion motion along the polar axis, shown in Fig. 3, was proposed. It was suggested that if the magnitudes of U and V_0 were such that the Nb ion is confined mostly to the lower-energy well, the motion between the two inequivalent wells would be characterized by two relaxation times which correspond to the two dwell times. The following expression was developed for the temperature dependence of the relaxation times:

$$\tau=\tau_0 \exp\left[\frac{\Delta V-kT}{kT_0}\right], \tag{23}$$

where $(\tau_0)^{-1}$ is the tunneling attempt frequency, ΔV is the barrier height, kT_0 is related to the Nb-ion mass and the curvature of the barrier, and kT is the average Nb-ion energy.

We would normally expect a simple double-well system to display only one relaxation time for return to equilibrium from population fluctuations in either direction, and therefore to give rise to a single feature in LS or ISS data. We propose an alternate explanation for the two relaxation times observed. In the orthorhombic phase, there are two lowest-energy "allowed" sites. A set of four sites has a somewhat higher energy, and another pair of sites has still higher energy. We propose that the two relaxation times observed are due to hopping between an allowed site and either of the two types of higher-energy sites. This offers a natural explanation of the observations which is consistent with all the features of the eight-site model.

According to this picture, the height $\Delta V'$ of the potential-energy barriers between the allowed sites and one set of higher-energy sites can be deduced from the temperature dependence of the faster relaxation time with an Arrhenius model,

$$\tau=\tau_0 \exp\left[\frac{\Delta V'}{kT}\right]. \tag{24}$$

The vibrational frequency in these higher-energy sites is approximately given by τ_0. Since most of the Nb ions are

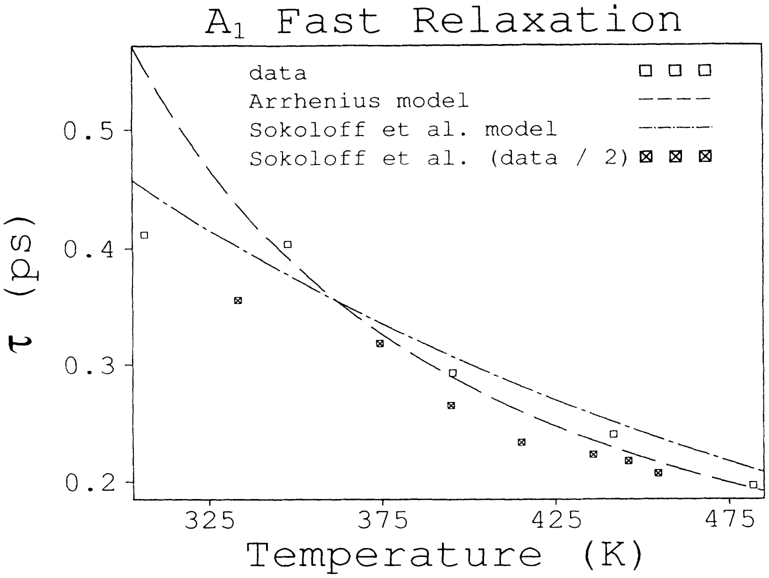

FIG. 16. The fast A_1-symmetry relaxation time as a function of temperature. Our results and the results of Sokoloff *et al.* (Ref. 3) are shown. The value of τ measured by our experiment is approximately half that from the Raman experiments (see text). Fits of the results to an Arrhenius from [Eq. (24)] and to Eq. (23) are shown.

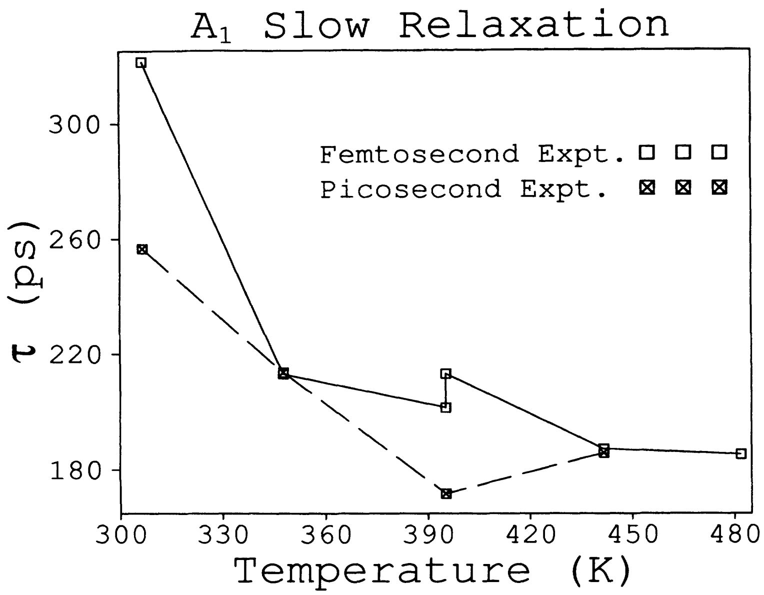

FIG. 17. Estimated values of the slow A_1-symmetry relaxation time as a function of temperature. The results of experiments using 70-fs and 90-ps pulses are shown. The values are only determined semiquantitatively, but their temperature-dependent trend is suggested.

in the allowed sites, the hopping rate from the higher-energy sites must be much greater than the hopping rate from the "allowed" sites, and τ will be dominated by the hopping from the excited well. The results of fitting the data to this model are shown in Fig. 16. The potential barrier height is 610 cm^{-1} and the attempt frequency is 170 cm^{-1} (i.e., the average time between attempts is $\tau_0=31$ fs). In fitting the fast relaxation the lowest-temperature data point was ignored. As Sokoloff *et al.* noticed, the Arrhenius model does not fit the temperature dependence of the fast relaxation data well near room temperature. A fit of the relaxation times, including the lowest-temperature point, to Eq. (23) (from Ref. 3) is shown in Fig. 16 and yields the results $\Delta V=620$ cm^{-1}, $\tau_0=35$ fs, and $kT_0=160$ cm^{-1}. The values for Δv and τ_0 are very similar to those found with the Arrhenius model. However, we do not consider them well determined over this limited temperature range.

Improved characterization of the two relaxation times (especially the longer one) would be useful since it would yield better quantitative characterization of the temperature-dependent potential-energy surface along which the central ion moves. The present results permit rough characterization of the projection of this surface along the directions between allowed sites and one class of higher-energy sites. Regarding the eight-site model, the A_1-symmetry results show the expected number and character of modes of this symmetry.

F. A_1 symmetry ISRS data from $BaTiO_3$

For the cases of $BaTiO_3$, two central peaks were detected in Raman spectra[3] designed to probe modes of A_1 symmetry. The broader (~600 GHz) peak was determined to be contaminated by leakage from the E-symmetry soft mode, but it was believed that some genuine A_1 contribution also was present. A narrow (<5 GHz) feature was determined to be a second distinct mode of A_1 symmetry. These results were similar to those from the orthorhombic phase of $KNbO_3$. However, within the framework of the eight-site model, only one relaxational mode should appear in the tetragonal phase since only one set of higher-energy sites exists.

ISRS data recorded to observe relaxational responses of A_1 symmetry showed an electronic response at $t=0$ but no lattice response whatsoever. We believe that the absence of nuclear signal is due to weak scattering intensity, but that some useful conclusions may be drawn from the nonobservation through comparison to A_1 ISRS and Raman[3] results from $KNbO_3$. In $KNbO_3$, ISRS data showed both fast and slow relaxational responses corresponding to the broad (~600 GHz) and narrow (<5 GHz) features observed in the Raman spectrum. The faster response gave rise to intense ISRS signal, but the slower response could barely be detected. We believe that the broad central feature observed in the Raman spectrum of $BaTiO_3$ is due entirely, not just partly, to leakage of E-symmetry scattering. It is very unlikely that such an A_1-symmetry mode, which by direct analogy to $KNbO_3$ should give rise to strong ISRS signal with a rapid but easily measurable decay rate, would escape detection in our experiments. However, the ISRS polarization selectivity is superior to that of Raman spectroscopy in that both the excitation polarizations and the probing and signal polarizations are used to select for A_1 modes.[27] Thus, the ratio of the E-symmetry leakage intensity to the A_1-symmetry signal collected in the A_1-symmetry ISRS geometry would be the square of the corresponding ratio in the Raman spectrum. On the other hand, the slow relaxational feature in $BaTiO_3$ is expected to be weak, again by direct analogy to $KNbO_3$ (see the Appendix). The ISRS signal-to-noise ratio in $BaTiO_3$ is also lower than in $KNbO_3$. Thus a slow relaxational mode could well escape detection in our ISRS experiments.

V. CONCLUSIONS

The first time-resolved ISRS observations of soft-mode dynamics in crystals near structural phase transitions have been carried out. The advantages of the time-domain approach for study of these heavily damped responses are clear, especially when the possible presence of other low-frequency contributions is an issue. We note that soft modes are characteristically heavily damped or overdamped near T_c, and the time-domain methods used here could be applied profitably to many materials.

In the present case, ISRS data for $KNbO_3$ clearly rule out relaxational contributions of B_2 symmetry. In addition, the soft-mode parameters determined from ISRS data yield a quantitative description of the $KNbO_3$ lattice dynamics which is consistent with dielectric behavior determined independently. According to this description, the polarization dynamics along the b crystallographic axis of the orthorhombic phase are displacive in nature, mediated by the soft-mode and higher-frequency modes, with no order-disorder character.

For the case of $BaTiO_3$, the data also rule out any possibility of significant relaxational (order-disorder) contributions of the same symmetry as the soft mode. We believe that the present results remove the last significant doubts concerning the eight-site model for structural phase transitions in this crystal class. We believe that this model will likely provide the framework for an accurate description of many transitions in this family.

Two relaxational modes of A_1 symmetry were observed in ISRS data for $KNbO_3$ as in earlier Raman spectra. We propose that these correspond to hopping motions of the Nb ion between the lowest-energy sites and the two sets of higher-energy sites. Our results and interpretation indicate hopping dynamics and order-disorder character for the polarization along the a and c crystallographic axes of the orthorhombic phase of $KNbO_3$. According to our interpretation, only one relaxational mode of A_1 symmetry is expected to be observed in the tetragonal phase of $BaTiO_3$. Although we did not observe this mode, we believe it to be a very weak scatterer (see the Appendix).

ACKNOWLEDGMENTS

The authors wish to thank J. P. Sokoloff and L. L. Chase for providing additional information concerning their light-scattering experiments. We also wish to thank C. Foster for providing the recent dielectric measurements on $BaTiO_3$ before publication. This work was supported in part by NSF Grant No. DMR-9002279 and by contributions from DuPont and Perkin-Elmer.

APPENDIX: COMPARISON OF TIME- AND FREQUENCY-DOMAIN SCATTERING INTENSITIES

Under ideal conditions the time- and frequency-domain Raman responses of relaxational modes reduce to simple forms which are readily compared. The relations can be used to estimate the relative signal intensities of two modes in an ISRS experiment from their relative peak intensities in frequency-domain light-scattering experiments and vice versa.

The frequency-domain Raman spectrum $I_F(\omega)$ for a single relaxational mode in the limit of perfect frequency and wave-vector resolution has the form

$$I_F(\omega) \propto An(\omega)G''(\omega) = \frac{An(\omega)\omega\tau}{1+(\omega\tau)^2} , \tag{A1}$$

where A is the scattering cross section, $n(\omega)$ is the Bose-Einstein thermal occupation factor, and $G''(\omega)$ is the imaginary part of the response function $G(\omega) = (1-i\omega\tau)^{-1}$ with τ the relaxation time.

The ISRS scattering intensity $I_T(t)$ for a single relaxational mode has the form[27]

$$I_T(t) \propto |AG(t)|^2 = \left[\frac{A}{\tau}\right]^2 e^{-2t/\tau} \tag{A2}$$

in the limit of perfect time and wave-vector resolution.

The peak intensities in the LS spectra and the ISRS data under ideal conditions reduce to very simple forms which can be used to assist in the interpretation of experiments when results from both techniques are available. From Eq. (A2), the ratio of the ISRS amplitudes, R_T, has the following form:

$$R_T = \left[\frac{A_1\tau_2}{A_2\tau_1}\right]^2 , \tag{A3}$$

where the subscripts identify the two different modes. From Eq. (A1), the ratio R_F of the peak Raman amplitudes at zero-frequency shift has the following form:

$$R_F = \frac{A_1\tau_1}{A_2\tau_2} . \tag{A4}$$

In the case of $BaTiO_3$, two relaxational modes with 600 GHz and 5-GHz linewidths were reported from A_1-symmetry Raman spectra.[3] From Eqs. (A3) and (A4) it can be seen that

$$R_T = R_F\frac{A_1}{A_2}\left[\frac{\tau_2}{\tau_1}\right]^3 . \tag{A5}$$

Considering only the 100-fold difference in relaxation times (assuming comparable cross sections A_i), the time-domain ratio of intensities R_T differs from the frequency-domain R_F ratio by a factor of 10^6. For this reason an intense, rapidly decaying (< 1 ps) signal would be expected in the ISRS data (as observed in $KNbO_3$) if the broad A_1 spectral feature were truly due to an A_1-symmetry mode and not to leakage of the E-symmetry spectrum. The narrower Raman feature, whose A_1 character is not in doubt, should appear as a much weaker slowly decaying response (also as seen in $KNbO_3$) in an ISRS experiment.

[1] M. E. Lines and A. M. Glass, *Principles and Applications of Ferroelectrics and Related Materials* (Clarendon, Oxford, 1977).

[2] T. P. Dougherty, G. P. Wiederrecht, and K. A. Nelson, Ferroelectrics **120**, 79 (1991); T. P. Dougherty, G. P. Wiederrecht, K. A. Nelson, M. H. Garrett, H. P. Jensen, and C. Warde, Science **258**, 770 (1992).

[3] J. P. Sokoloff, L. L. Chase, and D. Rytz, Phys. Rev. B **38**, 597 (1988); **40**, 788 (1989).

[4] E. Wiesendanger, Ferroelectrics **6**, 263 (1974).

[5] M. D. Fontana, A. Ridah, G. E. Kugel, and C. Carabatos-Nedelec, J. Phys. C **21**, 5853 (1988); Phys. Rev. B **40**, 786 (1989).

[6] W. Cochran, Adv. Phys. **9**, 387 (1960).

[7] P. W. Anderson, in *Fizika Dielektrikov,* edited by G. I. Skanavi (Akademii Nauk SSR, Moscow, 1960), p. 290.

[8] W. G. Spitzer, R. C. Miller, D. A. Kleinman, and L. E. Howarth, Phys. Rev. **126**, 1710 (1962).

[9] A. S. Barker, Jr., Phys. Rev. **145**, 391 (1966).

[10] Y. Luspin, J. L. Servoin, and F. Gervais, J. Phys. C **13**, 3761 (1980).

[11] Y. Tominaga and T. Nakamura, Solid State Commun. **15**, 1193 (1974); J. Phys. Soc. Jpn. **39**, 746 (1975).

[12] M. DiDomenico, Jr., S. H. Wemple, S. P. S. Porto, and R. P. Bauman, Phys. Rev. **174**, 522 (1968); M. DiDomenico, Jr., S. P. S. Porto, and S. H. Wemple, Phys. Rev. Lett. **19**, 855 (1967).

[13] A. Scalabrin, A. S. Chaves, D. S. Shim, and S. P. S. Porto, Phys. Status Solidi B **79**, 731 (1977).

[14] G. Burns and F. H. Dacol, Phys. Rev. B **18**, 5750 (1978).

[15] T. S. Benedict and J. L. Durand, Phys. Rev. **109**, 1091 (1958).

[16] S. H. Wemple, M. DiDomenico, Jr., and I. Camlibel, J. Phys. Chem. Solids **29**, 1797 (1968).

[17] R. Comes, M. Lambert, and A. Guinier, C. R. Acad. Sci. Paris **226**, 959 (1968).

[18] R. Comes, M. Lambert, and A. Guinier, Solid State Commun. **6**, 715 (1968).

[19] G. Burns and F. H. Dacol, Ferroelectrics **37**, 661 (1981); Solid State Commun. **42**, 9 (1982).

[20] H. Vogt, J. A. Sanjurjo, and G. Rossbroich, Phys. Rev. B **26**, 5904 (1982).

[21] A. M. Quittet and M. Lambert, Solid State Commun. **12**, 1053 (1973).

[22] M. D. Fontana, G. Metrat, J. L. Servoin, and F. Gervais, J. Phys. C **16**, 483 (1984).

[23] A. M. Quittet, J. L. Servoin, and F. Gervais, J. Phys. (Paris) **42**, 493 (1980).

[24] V. K. Yanovskii, Sov. Phys. Solid State **22**, 1284 (1980).

[25] J. Handerek, A. Aleksandrowicz, and M. Badurski, Acta Pol. A **56**, 769 (1979).

[26] P. J. Edwardson, Phys. Rev. Lett. **63**, 55 (1989).

[27] Y.-X. Yan and K. A. Nelson, J. Chem. Phys. **87**, 6240; **87**, 6257 (1987).

[28] L.-T. Cheng and K. A. Nelson, Phys. Rev. B **37**, 3603 (1988); **39**, 9437 (1989).

[29] A. R. Duggal and K. A. Nelson, J. Chem. Phys. **94**, 7677 (1991); S. M. Silence, A. R. Duggal, L. Dhar, and K. A. Nelson, *ibid.* **96**, 5448 (1992).

[30] S. Ruhman, A. G. Joly, and K. A. Nelson, IEEE J. Quant. Electron. **24**, 460 (1988).

[31] V. J. Newell, F. W. Deeg, S. R. Greenfield, and M. D. Fayer, J. Opt. Soc. Am. B **6**, 257 (1989).

[32] H. Vanherzeele, Appl. Opt. **27**, 3608 (1988).

[33] J.-C. Baumert, J. Hoffnagle, and P. Günter, in *1984 European Conference on Optics, Optical Systems, and Applications,* edited by B. Bolger and A. Ferwerda, SPIE Proc. Vol. 492 (SPIE, Bellingham, WA, 1984), p. 374.

[34] R. Claus, L. Merten, and J. Brandmuller, *Light Scattering by Phonon-Polaritons* (Springer-Verlag, Berlin, 1975); G. Lamprecht and L. Merten, Phys. Status Solidi B **55**, 33 (1973).

[35] T. P. Dougherty, G. P. Wiederrecht, and K. A. Nelson, J. Opt. Soc. Am. B **9**, 2179 (1992).

[36] L. Laughman, L. W. Davis, and T. Nakamura, Phys. Rev. B **6**, 3322 (1973).

[37] D. Heiman and S. Ushioda, Phys. Rev. B **9**, 2122 (1974).

[38] P. D. Lazay and P. A. Fleury, in *Light Scattering in Solids,* edited by M. Balkanski (Flammarion, Paris, 1971), p. 406; P. A. Fleury and P. D. Lazay, Phys. Rev. Lett. **26**, 1331 (1971).

[39] P. S. Peercy and G. A. Samara, Phys. Rev. B **6**, 2748 (1972).

[40] Z. Li, M. Grimsditch, and S.-K. Chan, Ferroelectrics (to be published).